Balance between cell–substrate adhesion and myosin contraction determines the frequency of motility initiation in fish keratocytes

Erin Barnhart[a,1], **Kun-Chun Lee**[b,1], **Greg M. Allen**[a], **Julie A. Theriot**[a,c,2,3], **and Alex Mogilner**[d,e,2,3]

[a]Department of Biochemistry and Howard Hughes Medical Institute, Stanford University School of Medicine, Stanford, CA 94305; [b]Department of Neurobiology, Physiology and Behavior, University of California, Davis, CA 95616; [c]Department of Microbiology and Immunology, Stanford University, Stanford, CA 94305; and [d]Courant Institute of Mathematical Sciences and [e]Department of Biology, New York University, New York, NY 10012

Edited by Herbert Levine, Rice University, Houston, TX, and approved March 11, 2015 (received for review September 9, 2014)

Cells are dynamic systems capable of spontaneously switching among stable states. One striking example of this is spontaneous symmetry breaking and motility initiation in fish epithelial keratocytes. Although the biochemical and mechanical mechanisms that control steady-state migration in these cells have been well characterized, the mechanisms underlying symmetry breaking are less well understood. In this work, we have combined experimental manipulations of cell–substrate adhesion strength and myosin activity, traction force measurements, and mathematical modeling to develop a comprehensive mechanical model for symmetry breaking and motility initiation in fish epithelial keratocytes. Our results suggest that stochastic fluctuations in adhesion strength and myosin localization drive actin network flow rates in the prospective cell rear above a critical threshold. Above this threshold, high actin flow rates induce a nonlinear switch in adhesion strength, locally switching adhesions from gripping to slipping and further accelerating actin flow in the prospective cell rear, resulting in rear retraction and motility initiation. We further show, both experimentally and with model simulations, that the global levels of adhesion strength and myosin activity control the stability of the stationary state: The frequency of symmetry breaking decreases with increasing adhesion strength and increases with increasing myosin contraction. Thus, the relative strengths of two opposing mechanical forces—contractility and cell–substrate adhesion—determine the likelihood of spontaneous symmetry breaking and motility initiation.

symmetry breaking | cell migration | adhesion | myosin

Stationary adherent cells are symmetric systems, in which all forces generated by and acting on the cell are balanced, allowing the cell to maintain a consistent shape and position. In order for a stationary cell to initiate motility, the symmetry of the system must first be broken by external or internal cues. Mechanisms of symmetry breaking have been extensively studied in chemotactic cells, such as neutrophils and *Dictyostelium*, which break symmetry and migrate in the direction of chemoattractant gradients (1). However, stationary neutrophils also break symmetry and initiate motility in uniform baths of chemoattractant (2, 3), indicating that a directional cue is not required. In addition, nonchemotactic cells, including fish epithelial keratocytes and keratocyte fragments, are able to break symmetry and initiate motility in the absence of external cues (4, 5). Thus, while external cues may confer a preferred directionality, intrinsic cellular instabilities can be sufficient for symmetry breaking.

Spontaneous symmetry breaking requires nonlinear amplification of stochastic fluctuations in chemical or mechanical signals (6). To understand how cellular systems break symmetry, it is necessary to answer three questions. First, what are the relevant fluctuations that drive symmetry breaking? Second, how are those fluctuations amplified in time and space? Finally, what sets the instability threshold—i.e., what determines the magnitude of the initial fluctuations that are required before the system breaks symmetry? Feedback between diffusible chemical activators and inhibitors can trigger biochemical instabilities (often called “Turing instabilities”) that result in symmetry breaking (7); notable cellular examples include Min protein oscillations in *Escherichia coli* (8) and polarization and symmetry breaking in budding yeast (9). Mechanical instabilities can also drive symmetry breaking and have been shown to be particularly relevant for force-generating cytoskeletal systems (10–12). Stochastic fluctuations in actin filament densities and mechanical feedback between motor proteins and cytoskeletal elements can drive symmetry breaking, as in reconstituted actin-based rocketing motility of bacterial pathogens (13–15) and during asymmetric division of the *Caenorhabditis elegans* embryo (16, 17). Synthetic biology experiments have shown that both positive feedback and mutual inhibition are sufficient for symmetry breaking under limited conditions; combining multiple feedback loops promotes symmetry breaking under broader sets of conditions (18).

Feedback among multiple mechanical systems is likely to contribute to symmetry breaking and initiation of cell migration (5). Symmetry breaking is associated with rearrangement of actin polymerization and actin network flow patterns (5), and stochastic fluctuations in the mechanical systems that govern either actin polymerization or flow could, in principle, trigger symmetry breaking. Previous work has shown that increased myosin activity

Significance

Symmetry breaking and motility initiation are required for many physiological and pathological processes, but the mechanical mechanisms that drive symmetry breaking are not well understood. Fish keratocytes break symmetry spontaneously, in the absence of external cues, with myosin-driven actin flow preceding rear retraction. Here we combine experimental manipulations and mathematical modeling to show that the critical event for symmetry breaking is a flow-dependent, nonlinear switch in adhesion strength. Moreover, our results suggest that mechanical feedback among actin network flow, myosin, and adhesion is sufficient to amplify stochastic fluctuations in actin flow and trigger symmetry breaking. Our mechanical model for symmetry breaking in the relatively simple keratocyte provides a framework for understanding motility initiation in more complex cell types.

Author contributions: E.B., J.A.T., and A.M. designed the experiments; E.B. and G.M.A. performed the experiments; E.B. analyzed the data; K.-C.L. and A.M. wrote the mathematical model and carried out model simulations; and E.B., J.A.T., and A.M. wrote the paper.

The authors declare no conflict of interest.

This article is a PNAS Direct Submission.

[1] E.B. and K.-C.L. contributed equally to this work.

[2] J.A.T. and A.M. contributed equally to this work.

[3] To whom correspondence may be addressed. Email: mogilner@cims.nyu.edu or theriot@stanford.edu.

This article contains supporting information online at www.pnas.org/lookup/suppl/doi:10.1073/pnas.1417257112/-/DCSupplemental.

in the prospective cell rear of stationary fish keratocytes results in increased centripetal flow of the actin network, rear retraction, and motility initiation (5), and myosin contraction has been shown to contribute to symmetry breaking by defining the cell rear in other cell types as well (19, 20). Moreover, myosin II minifilaments bind and move with the actin network, resulting in positive feedback between myosin localization and actin network flow: Myosin activity drives actin flow, resulting in the accumulation of more actin-bound myosin. This positive feedback between myosin and actin flow is thought to be required for symmetry breaking in fish keratocytes (5).

The forces generated by myosin-dependent actin flow are transmitted to the substrate by adhesion complexes, but the manner in which adhesions contribute to symmetry breaking is not well understood. Cell–substrate adhesions are dynamic structures, composed of molecules that link the actin network to adhesion receptors on the cell surface, which, in turn, bind to ligands on the substrate (21). The dynamic coupling of the actin network with the underlying substrate, via populations of adhesion molecules, generates a frictional slippage interface between the cell and the surface (22). Forces generated by myosin-dependent actin flow are transmitted to the substrate via this frictional interface, resulting in traction force generation. We have previously found that alterations in cell–substrate adhesion change the magnitude of myosin-driven actin network flow in motile keratocytes (23), raising the question of how variations in cell–substrate adhesion might contribute to changes in the spatial pattern of actin network flow during the process of symmetry breaking and motility initiation for stationary cells.

In this work, we have combined traction force measurements with experimental manipulations of cell–substrate adhesion and myosin activity and mathematical modeling to understand the contribution of adhesion- and myosin-dependent feedback loops to symmetry breaking and motility initiation in fish keratocytes. Our model simulations and experimental evidence suggest that stochastic fluctuations in adhesion strength and myosin activity trigger an actin flow-dependent, nonlinear switch in adhesion strength that results in symmetry breaking and persistent motility.

Results

Stationary Cells Have Stronger Adhesions Than Motile Cells. Stationary, radially symmetric keratocytes exhibit slow centripetal actin network flow (5). Slow actin network flow can be associated with either weak traction force generation or strong traction force generation, depending on the state of the adhesions (24). To determine whether stationary keratocytes are in a low-traction or high-traction regime, we first set out to characterize the spatial organization of the adhesion–contraction force balance system in stationary and motile keratocytes under comparable conditions. To do this, we directly measured traction force and actin flow patterns for cells in both configurations, as well as the distribution of myosin II and adhesion-related proteins (Fig. 1). To measure traction forces in stationary and motile cells, we plated keratocytes on polyacrylamide (PAA) gels with fluorescent beads embedded in the top layer of the gel and measured traction stress fields from cell-induced bead displacements (25). We found that motile keratocytes primarily exert traction forces perpendicular to the direction of cell movement, with slight rearward traction forces at the cell front (Fig. 1*A*), consistent with previous work (26, 27). Stationary cells, in contrast, display centripetal traction force patterns (Fig. 1*A*). Stationary cells generate substantially higher traction forces (average traction force = 46.2 Pa, $n = 10$ cells) compared with motile cells (28.8 Pa at the leading edge, and 7.7 Pa in the rear, $n = 9$ cells; Fig. 1*F*). Adhesions in stationary cells are also larger and more elongated than adhesions in motile cells (Fig. 1*C*).

Next, we used quantitative actin speckle microscopy (5, 28) to measure actin network flow (Fig. 1 *B* and *G*). We found, as previously described (5, 28), that whereas stationary keratocytes were characterized by slow, centripetal flow of the actin network (average flow rate = 37 ± 4 nm/s, $n = 3$ cells), motile keratocytes were characterized by rapid inward flow of the actin network in the cell rear (267 ± 43 nm/s, $n = 3$ cells) and slow retrograde flow at the leading edge (65 ± 3 nm/s). In both stationary and motile cells, myosin was enriched in regions of the cell that exhibit the most retrograde flow (Fig. 1 *D* and *I*)—to a ring around the cell body in stationary cells and to either side of the cell body in the cell rear in motile cells—consistent with the well-established idea that there is positive feedback between local myosin concentration or activity and actin network flow (5, 23, 28).

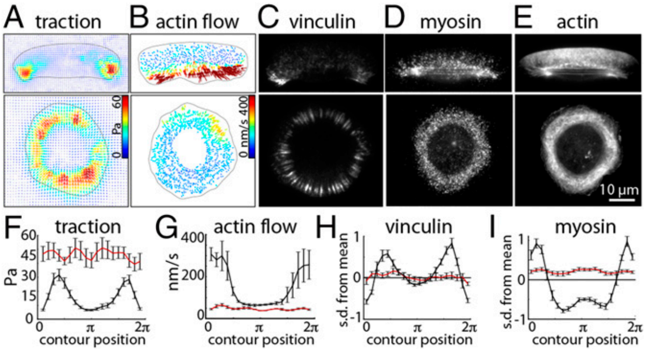

Fig. 1. Traction force, actin flow, adhesion, and myosin distributions in motile and stationary cells. (*A* and *B*) Traction stress maps (*A*) and actin flow maps (*B*) for motile (*Top*) and stationary (*Bottom*) keratocytes. Arrows indicate the direction and magnitude of the traction forces (*A*) and actin network movement with respect the underlying substrate (*B*); hot colors indicate faster flow. (*C*–*E*) Images of motile (*Top*) and stationary (*Bottom*) keratocytes immunolabeled for the adhesion protein vinculin (*C*, total internal reflection fluorescence images) or myosin (*D*, epifluorescence images) or labeled for actin with fluorescent phalloidin (*E*, epifluorescence images). (*F*–*I*) Average traction force (*F*), actin flow (*G*), vinculin (*H*), and myosin (*I*) distributions in motile (black line) and stationary (red line) cells are plotted versus cell boundary position. Fluorescent intensities were normalized for each cell by subtracting the mean intensity and dividing by the SD. Error bars are SEM. The images of motile cells in *A*–*E* are oriented with the leading edge pointed toward the top of the page.

These results also suggest a second form of nonlinear feedback—in addition to positive feedback between myosin activity and actin network flow—that could contribute to symmetry breaking in keratocytes. Specifically, we observe that the relationship between actin network flow and traction force generation is different in stationary and motile cells (Fig. 1 *A*, *B*, *F*, and *G*). Stationary cells generate large traction forces and exhibit slow actin network flow, whereas motile cells generate relatively small traction forces despite much faster flow rates. This indicates that the adhesive coupling between the actin network and the underlying surface is lower in the rear of motile cells than in stationary cells, suggesting that adhesions in the prospective cell rear must weaken or break during symmetry breaking in stationary cells. An actin flow-dependent nonlinear switch in adhesion strength has been previously observed in mammalian epithelial cells, with the adhesive coupling between the substrate and the actin network decreasing at a critical actin flow rate (24). We therefore hypothesize that, in keratocytes, negative feedback between actin flow and adhesions in the prospective cell rear in the form of a nonlinear switch in their coupling, as well as positive feedback between flow and myosin, may drive retraction of the cell rear and motility initiation (Fig. 2 *A* and *B*).

A Nonlinear Switch in Adhesion Strength Is Required for Motility Initiation. To understand how these two distinct feedback loops might contribute to symmetry breaking, we set out to develop a general computational model for the balance between myosin

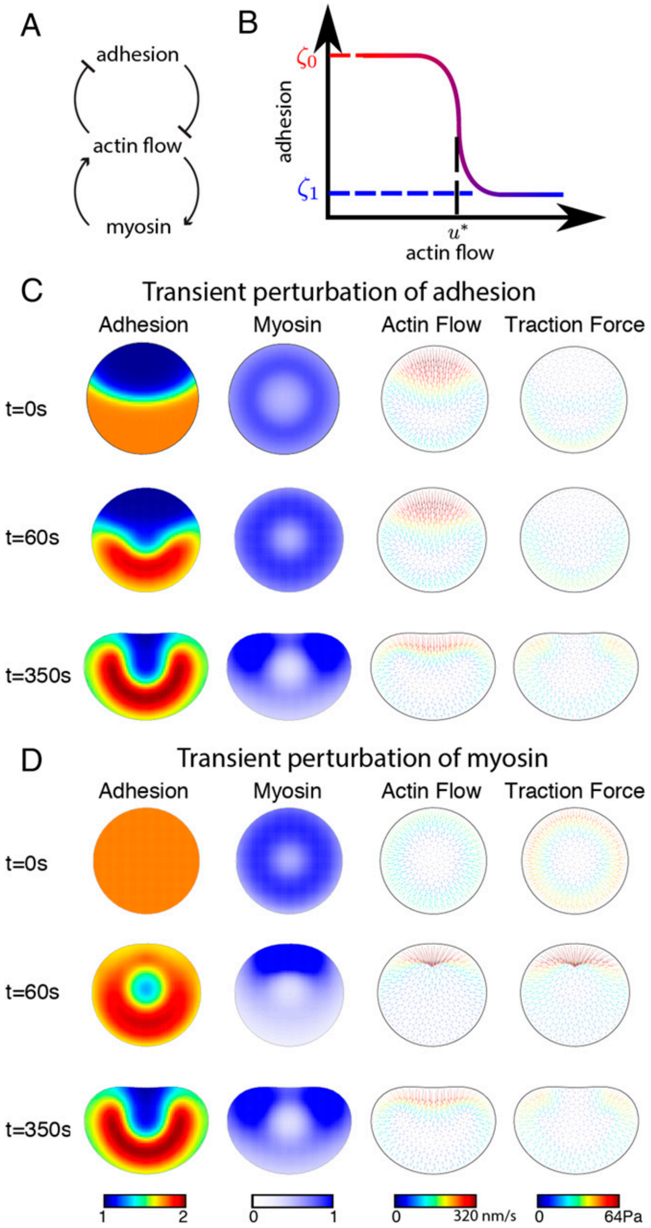

Fig. 2. Simulated traction force, actin flow, adhesion, and myosin distributions in response to transient asymmetries in adhesion strength or myosin density. (*A*) Model simulations incorporate two feedback loops: positive feedback between actin network flow and myosin density and negative feedback between actin flow and adhesion strength. (*B*) Negative feedback between actin flow and adhesion strength is modeled as an actin flow-dependent, nonlinear switch in adhesion strength. Adhesion strength decreases from ζ_0 to ζ_1 when actin flow rates exceed a critical threshold, u^*. (*C* and *D*) Simulated adhesion, myosin, actin flow, and traction force distributions after transient perturbation of adhesion (*C*) or myosin (*D*). The details of the model simulations are described in *SI Text*. In brief, the model simulations were initiated with a circular cell with a fixed boundary and uniform adhesion ($\zeta = \zeta_0$) and myosin densities. The cell boundary was fixed for the first 2 min of the simulation to allow myosin densities and actin flow patterns to equilibrate. Then, the strength of adhesion was reduced (*C*) or the myosin density was increased (*D*) on one side of the cell ($t = 0$ s). Adhesion, myosin, and actin flow patterns were then allowed to evolve according the rules governing feedback among actin flow, adhesion strength, and myosin density for 1 min. The external adhesion and myosin asymmetries were removed, and the cell boundary was released and allowed to move according to the simulated actin flow patterns ($t = 60$ s). Transient perturbation of either adhesion strength or myosin density resulted in persistent, rapid movement of fan-shaped cells ($t = 350$ s).

contraction and adhesion forces applicable to both motile and stationary cells. Our model builds on a recently published model for myosin-driven retrograde flow of the actin network in motile keratocytes (23, 29), described in detail in *SI Text* and Tables S1 and S2. In the context of this model, populations of dynamic adhesion bonds create a frictional slippage interface between the actin network and the underlying surface, generating traction force (21, 22). We assume, therefore, that traction force magnitudes depend on the effective friction coefficient between the cell and the substrate—determined by the number and strength of adhesion bonds—and the rate of actin network flow, relative to the underlying substrate: $\vec{T} = \zeta\vec{U}$. $\vec{T}$ is the traction force exerted by the cell on the underlying substrate through adhesions, ζ is the effective adhesion friction coefficient, and $\vec{U}$ is the rate of actin network flow. Based on our observations of the difference in coupling between actin network flow and traction force between stationary cells (with slow flow and high traction) and at the rear in motile cells (with rapid flow and weak traction), we postulate an actin flow-dependent, nonlinear switch in adhesion strength, as previously observed in mammalian epithelial cells (24), such that the adhesion drag coefficient ζ decreases dramatically when actin flow rates reach a critical threshold (Fig. 2*B*). Based on our actin flow measurements (Fig. 1 *B* and *G*), realistic values for this critical flow rate range from 100 nm/s (greater than the flow rate in stationary cells and at the front in motile cells) to 200 nm/s (less than the flow rate at the rear in motile cells); for our model, we set the critical flow rate to 150 nm/s.

To couple adhesion and traction to myosin activity, we note that, generally, myosin-generated contractile forces are balanced by traction forces: $k\nabla m = \vec{T}$. In this equation, m is the myosin density, k is a proportionality coefficient describing the amount of force produced per myosin unit, and $k\nabla m$ is the gradient of the isotropic myosin-generated stress proportional to the myosin density. In our full model, myosin contraction is also balanced by passive viscous resistance from actin network deformations (see *SI Text*).

In this model, the spatiotemporal distribution of contractile forces, actin network flow, and traction forces depends on the spatiotemporal regulation of the myosin density (m), the amount of force produced by myosin (k), the adhesion friction coefficient (ζ), and the actin network viscosity (η; see *SI Text*). For simplicity, we assume that k and η are constant in space and time, although these are not necessary assumptions. To model the myosin density distribution, we assume, based on previous work (23, 29), that myosin minifilaments bind and move with the actin network (*SI Text*), resulting in positive feedback between myosin localization and actin network flow: As myosin molecules accumulate on the actin network, increased myosin contraction results in increased actin flow and the delivery of additional actin-bound myosin minifilaments.

To determine whether this model, which incorporates negative feedback between actin network flow and adhesion strength in the form of a nonlinear switch, can account for symmetry breaking and motility initiation in response to local up-regulation of myosin activity or local inhibition of adhesion strength, we performed free-boundary model simulations. In these simulations, the cell boundary evolves over time in response to the balance of actin polymerization and inward flow rates. Specifically, the cell boundary remains stationary when actin polymerization and flow rates are equal, protrudes when polymerization is greater than inward flow, and retracts when flow is greater than polymerization (*SI Text*). For simplicity, actin polymerization is maintained at a constant rate in our stimulations (although this is not a necessary assumption), whereas actin flow rates increase with increasing myosin activity and decreasing adhesion strength, in accordance with the model described above. We simulated the effects of either a transient reduction of the adhesion drag coefficient ζ on one side of a stationary cell (Fig. 2*C*) or a transient increase in the myosin concentration (Fig. 2*D*). In these simulations, reduced adhesion strength and increased myosin activity both resulted in increased actin flow in the cell rear, followed by symmetry breaking and the initiation of persistent motility. Reduced adhesion resulted in immediate and persistent reduction of traction forces in the cell rear, whereas increased myosin caused traction forces in the prospective cell rear to briefly increase before decreasing. Additional model simulations that did not incorporate the actin flow-dependent nonlinear switch in adhesion strength failed to produce realistic symmetry breaking (Figs. S1 and S2; see *SI Text*), suggesting that negative feedback between adhesion and actin flow is required for motility initiation.

A Reduction in Adhesion Strength Immediately Precedes Spontaneous Symmetry Breaking. Our model simulations thus far suggest that transient asymmetries in either myosin density or adhesion strength can trigger symmetry breaking. These predictions, however, are based on simulations in which relatively large and long-lasting asymmetries in adhesion and myosin density are added as external triggers to the model. To determine whether stochastic local fluctuations in either adhesion strength or myosin activity could be amplified by the feedback loops intrinsic to our model to trigger whole-cell symmetry breaking, we added fluctuations to our free-boundary simulations (*SI Text*). In brief, we added spatial–temporal fluctuations of the actin flow to the equations that describe the dynamics of the adhesion drag coefficient, the myosin density, or both. We found that stochastic fluctuations in actin flow rates can trigger spontaneous symmetry breaking and persistent motility (Fig. 3*A* and Fig. S3). The simulated distributions of traction force, actin flow, and myosin density following symmetry breaking were consistent with experimental measurements of these distributions in motile cells (compare Fig. S4 *A*–*C* and Fig. 1 *F*, *G*, and *I*). A switch in the relationship between traction force and actin flow in the cell rear compared with the cell sides and front was likewise consistent with experimental measurements: Traction forces increased with increasing actin flow rates from the center of the leading edge around the cell perimeter to the sides of the rear but decreased in the center of the rear where flow rates are highest (Fig. S5).

In our simulations, symmetry breaking occurred when local fluctuations persisted for a few tens of seconds and were correlated in space over a few microns (*SI Text*), and model cells that exhibited more variability in traction forces were more likely to break symmetry (Fig. S6). We also found that while the precise time course for the evolution of traction forces during symmetry breaking was variable—either increasing or decreasing in the 5 min before motility initiation, depending on the source of the stochastic fluctuations (see *SI Text*)—in all cases, traction forces and adhesion strength significantly increased and actin flow significantly decreased in the minute before motility initiation (Fig. 3*B* and Fig. S4 *D* and *E*).

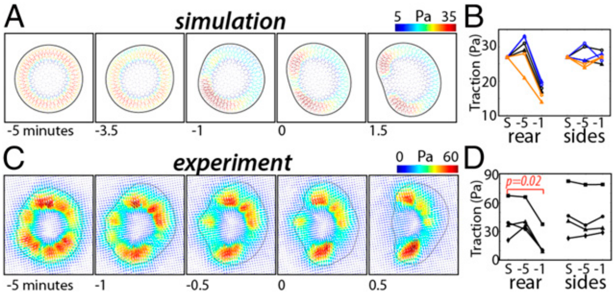

Fig. 3. Traction forces decrease in the prospective rear before motility initiation. (*A* and *C*) Simulated (*A*) and experimental (*C*) traction force maps; arrows indicate direction and magnitude of traction forces. (*B* and *D*) Traction force measurements from six simulations (*B*) and four real cells (*D*). Traction forces in the prospective cell rear and sides are plotted for the start of the simulation or the first imaging frame (S) and 5 min and 1 min before the onset of stable motility (−5 and −1, respectively). For the simulations, stochastic fluctuations were added to actin flow in the dynamic equations for myosin localization (blue lines), adhesion strength (orange lines), or both (black lines).

These model simulations generated two testable predictions: First, cells that break symmetry should be characterized by more variable traction forces before symmetry breaking compared with cells that remain stationary. Second, traction forces should decrease in the prospective rear immediately before the onset of persistent cell motility. To test these predictions, we measured traction forces generated by nine stationary keratocytes for up to 1 h to determine how traction forces evolve over the course of symmetry breaking (Fig. 3 *C* and *D*). Four of the nine cells initiated motility, and two remained stationary. The remaining three cells exhibited persistent, fluctuating shape changes in the absence of persistent movement; these "shape-shifters" were excluded from subsequent analysis. Cells that remained stationary and those that initiated motility displayed the same average traction force magnitudes, but the SD in forces was significantly higher in cells that initiated motility (Fig. S6 *B*–*D*), consistent with our first model prediction. Finally, traction forces in the prospective rear decreased in the minute before motility initiation in all four cells, consistent with our second model prediction (Fig. 3*D*, $P = 0.02$, paired t test).

Taken together, the model simulations and traction force measurements described above suggest that an actin flow-dependent reduction in adhesion strength triggers motility initiation. If this is the case, then local inhibition of cell–substrate adhesion should drive symmetry breaking and motility initiation in stationary cells. To test this, we inhibited adhesion on one side of a stationary keratocyte by local application of soluble peptides containing the RGD (Arg-Gly-Asp) integrin-binding motif (30) with a micropipet (Fig. 4 *A* and *C*). Consistent with our prediction, we found that 31% of cells initiated motility, 62% retracted away from the needle, and 7% remained stationary ($n = 13$ cells). Cells that initiated motility continued to move even after the micropipet was removed. Local application of fluorescent dextrans did not induce motility initiation or retraction ($n = 5$ cells). Moreover, we found that local application of soluble RGD peptides to cells that were pretreated with the myosin II inhibitor blebbistatin also induced symmetry breaking and initiated motility (Fig. 4 *B* and *C*): 50% of the cells initiated motility, 33% retracted from the needle, and 17% remained stationary ($n = 6$ cells). Thus, reduced adhesion strength is sufficient for motility initiation even when myosin contraction is inhibited.

The Frequency of Motility Initiation Depends on the Balance Between Adhesion and Contractile Forces. In our model, the critical flow rate at which adhesions switch from sticking to slipping ($u^* =$ 150 nm/s) represents an instability threshold: Fluctuations that drive the actin flow rate above this threshold trigger negative feedback between actin flow and adhesion strength, eventually causing retraction of the cell rear and motility initiation. We have shown that local inhibition of adhesion triggers motility initiation (Fig. 4); we also predict that global levels of adhesion strength should have an effect on symmetry breaking. Specifically, when adhesion strength is high, the global actin flow rate is low, and vice versa (Fig. S7). As adhesion strength increases, relatively larger fluctuations in actin flow should be required to drive flow rates above the instability threshold, and the frequency of motility initiation should decrease. To test this idea, we plated keratocytes plated on surfaces coated with low, intermediate, or high densities of RGD peptides and measured the fraction of stationary cells that initiated motility after a temperature shift (5). As expected, we found that the frequency of motility initiation increased as adhesion strength decreased (Fig. 5*A*). In addition, since the relative levels of myosin activity and adhesion strength control actin flow rates (23), increasing or decreasing myosin activity should increase or

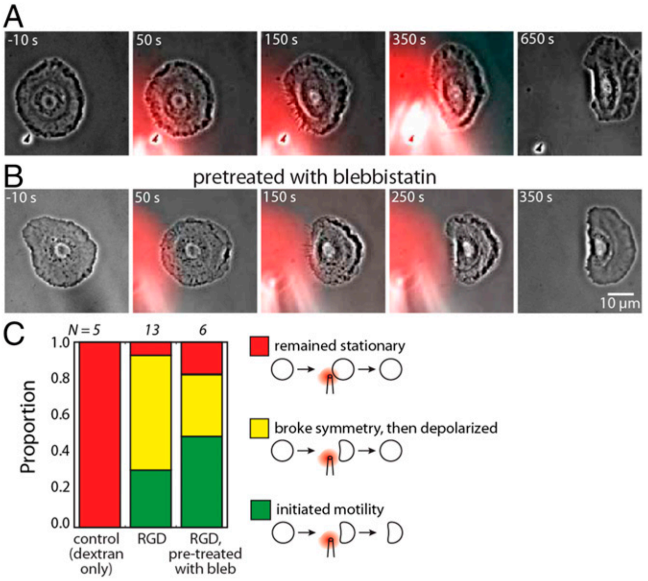

Fig. 4. Local inhibition of cell–substrate adhesion can drive motility initiation. (*A* and *B*) Soluble RGD peptides were applied near stationary cells using a micropipette. The cell in *B* was pretreated with 25 μM blebbistatin for 20 min before RGD application. The cells broke symmetry after RGD application (at $t = 0$ s) and migrated away from the microneedle; both cells maintained polarization and continued to migrate after the RGD peptides were removed (at 500 s in *A* and 275 s in *B*). Red pseudocolor indicates the flow of the RGD peptides away from the pipette. (*C*) The fraction of stationary cells that remained stationary (red), broke symmetry and then lost polarity (yellow), or initiated stable motility (green) after application of Texas Red (TR) dextran alone or TR dextran plus RGD peptides.

decrease the frequency of motility initiation in our temperature shift experiments on all substrates. To test this, we treated cells plated on low, medium, or high RGD densities with either blebbistatin, a myosin II inhibitor (31), or calcyculin A, a phosphatase inhibitor that promotes myosin activity (23, 32). Blebbistatin decreased the fraction of cells that initiated motility on all substrates, whereas calyculin A treatment increased the frequency of motility initiation (d).

Finally, we performed dynamic boundary simulations with stochastic fluctuations around various average myosin and adhesion strengths and, for each parameter set, observed whether the symmetric nonmotile shape remained stable or broke symmetry and initiated motility. These simulations recapitulate our experimental results: When adhesion strength is lowered or myosin is strengthened, the stability of the nonmotile state decreases, resulting in motility initiation (Fig. 5*B*). Altogether, our experimental results and model simulations are consistent with the idea that global adhesion- and myosin-dependent actin flow rates control symmetry breaking by determining how much actin flow fluctuations must be amplified before reaching the critical flow rate at which adhesions switch from gripping to slipping.

Discussion

The initiation of cell migration requires dramatic reorganization of multiple force-generating systems. Here we have presented a mechanical model for symmetry breaking and motility initiation in fish epithelial keratocytes in which stochastic fluctuations in adhesion- and myosin-dependent actin flow are amplified by a nonlinear, flow-dependent switch in adhesion strength. In this model, the critical actin flow rate at which adhesions switch from sticking to slipping sets an instability threshold. Local, stochastic fluctuations in actin flow, myosin localization, or adhesion strength that increase actin network flow above this critical threshold trigger negative feedback between flow and adhesion strength, thereby reducing adhesion strength and further increasing actin flow and myosin accumulation. Amplification of these initial fluctuations eventually results in levels of actin flow high enough to cause retraction of the cell rear and motility initiation.

This model depends on the existence of a nonlinear, flow-dependent switch in adhesion strength. Adhesions are both mechanical structures that transmit forces to the underlying substrate and signaling platforms that localize components of numerous biochemical signaling pathways (21). Rac and Rho GTPase, in particular, have been shown to control adhesion strength and cytoskeletal dynamics (33), and feedback between Rac and Rho signaling networks could, in principle, trigger an actin flow-dependent switch in adhesion strength. However, the critical flow rate for switching adhesions from sticking to slipping in mammalian epithelial cells is impervious to pharmacological perturbation of Rac and Rho GTPase (24), suggesting that signaling is not required for the switch. Instead, a purely mechanical mechanism may be sufficient. Cell–substrate adhesion is mediated by populations of adhesion molecules that link the actin network, through various molecular interactions, to the underlying surface (21). When the actin network moves relative to the underlying surface, these adhesion molecules stretch and detach from the surface with extension-dependent kinetics (34), thereby establishing a frictional slippage interface through which force is exerted on the underlying surface (22). Since adhesion is mediated by a population of adhesion molecules, when actin network flow is slow, a relatively large proportion of adhesion molecules remain bound to the underlying surface at any point in time, and the amount of force transmitted across an individual bond is relatively low. As actin network flow increases, however, fewer and fewer adhesion molecules remain bound to the surface at any point in time, and the amount of force transmitted across an individual bond increases. Eventually, the amount of force transmitted across each individual adhesion bond in the population becomes too great, resulting in detachment of these remaining bonds, and switching the adhesion as a whole from sticking to slipping. Thus, extension-dependent detachment of adhesion molecules, on its own, may be sufficient for an actin-flow-dependent switch in adhesion strength.

Our model for symmetry breaking incorporates two feedback loops: negative feedback between actin flow and adhesion and positive feedback between myosin contraction and actin flow. A recent synthetic biology study (18) suggests that cell polarization

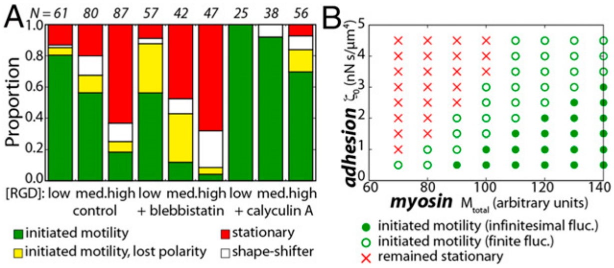

Fig. 5. The balance between myosin contraction and adhesion strength determines the frequency of motility initiation. (*A*) The stability of the symmetric, stationary state was assessed experimentally by measuring the fraction of stationary cells that initiated motility following a temperature shift. (*B*) Numerical simulations of cell boundary dynamics were carried out at the indicated values for ζ_0 (adhesion friction coefficient at low actin flow) and *M* (myosin concentration). At low adhesion or high myosin strength, the symmetric state is unstable (green circles—cells initiate motility instantly in simulations due to very small fluctuations), whereas at high adhesion or low myosin strength, the symmetric state is stable (red crosses). Open green circles indicate the adhesion and myosin strengths at which symmetry breaking requires finite-amplitude fluctuations and takes tens of minutes.

can be achieved by minimal motifs—i.e., positive feedback, or mutual inhibition—under limited conditions, but that circuits combining two or more motifs are significantly more robust. Consistent with this, our results suggest that a single feedback loop may be sufficient for symmetry breaking in stationary keratocytes under extreme conditions. Specifically, positive feedback between actin flow and myosin contraction may be sufficient for symmetry breaking when cell–substrate adhesion strength is low. The rate of actin flow in stationary keratocytes plated on surfaces coated with low densities of adhesion ligands is higher than the critical flow rate at which adhesions switch from sticking to slipping (Fig. S7). This suggests that adhesions in these stationary cells are all slipping, in which case, negative feedback between adhesion and actin flow would not contribute to symmetry breaking. However, these cells break symmetry much more readily than cells plated on surfaces coated with higher densities of adhesion ligands (Fig. 5*A*), suggesting that negative feedback between adhesion and actin flow is not required for symmetry breaking in keratocytes in a low-adhesion state. Our model simulations demonstrate that positive feedback between myosin and actin flow is sufficient for symmetry breaking, with motile cells assuming a nearly round morphology and slow migration speeds following symmetry breaking (Fig. S1), and motile keratocytes plated on surfaces coated with low-adhesion ligand densities are indeed round and slow moving (23). Therefore, it may be that positive feedback between myosin and actin flow is sufficient for symmetry breaking when cell–substrate adhesion strength is low, and that negative feedback between adhesion and flow becomes necessary when adhesion strength increases. Moreover, additional feedback loops, including signaling mechanisms as well as mechanical feedback, may be required for robust motility initiation in other cell types. On the whole, our mechanical model for motility initiation in the relatively simple keratocyte model system provides a framework for understanding symmetry breaking and self-organization phenomena in larger, more complex systems.

Experimental Methods

Keratocyte Culture. Keratocytes were cultured from the scales of the Central American cichlid *Hypsophrys nicaraguensis* as previously described (5).

Traction Force Measurements. RGD-functionalized PAA gels with fluorescent beads embedded near the surface were generated using a modified version of previously published protocols (*SI Text*). Traction forces were measured from cell-induced bead displacements using the Fourier transform traction cytometry method (25).

Actin Speckle Microscopy. The F-actin network in keratocytes was sparsely labeled by electroporation of AlexaFluor546 phalloidin (AF546-phalloidin; Invitrogen), and movement of the actin network relative to the underlying surface was measured using a previously published multiframe correlation algorithm (5, 28) (*SI Text*).

Computational Modeling. The model consists of coupled submodels for viscous flow of the actomyosin network, myosin transport, and adhesion density and strength. We solved the equations of these submodels (described in detail in *SI Text*) using the general public-licensed software FreeFem (available for download at www.freefem.org) designed to solve partial difference equations using finite element methods. The equations were solved on the free-boundary domain as described in *SI Text*.

Additional experimental methods are described in *SI Text*.

ACKNOWLEDGMENTS. We are grateful to Ulrich Schwarz for providing the MatLab code used to analyze traction forces, and to Cyrus Wilson and Gaudenz Danuser for providing the MatLab code used to track actin network flow. This study was supported by National Institutes of Health Grant GM068952 (to A.M.) and by a grant from Howard Hughes Medical Institute (to J.A.T.).

1. Iglesias PA, Devreotes PN (2008) Navigating through models of chemotaxis. *Curr Opin Cell Biol* 20(1):35–40.
2. Zigmond SH, Levitsky HI, Kreel BJ (1981) Cell polarity: An examination of its behavioral expression and its consequences for polymorphonuclear leukocyte chemotaxis. *J Cell Biol* 89(3):585–592.
3. Coates TD, Watts RG, Hartman R, Howard TH (1992) Relationship of F-actin distribution to development of polar shape in human polymorphonuclear neutrophils. *J Cell Biol* 117(4):765–774.
4. Verkhovsky AB, Svitkina TM, Borisy GG (1999) Self-polarization and directional motility of cytoplasm. *Curr Biol* 9(1):11–20.
5. Yam PT, et al. (2007) Actin-myosin network reorganization breaks symmetry at the cell rear to spontaneously initiate polarized cell motility. *J Cell Biol* 178(7):1207–1221.
6. Goehring NW, Grill SW (2013) Cell polarity: Mechanochemical patterning. *Trends Cell Biol* 23(2):72–80.
7. Turing AM (1952) The chemical basis of morphogenesis. *Philos Trans R Soc B* 237(641): 37–72.
8. Loose M, Fischer-Friedrich E, Ries J, Kruse K, Schwille P (2008) Spatial regulators for bacterial cell division self-organize into surface waves in vitro. *Science* 320(5877): 789–792.
9. Wedlich-Soldner R, Altschuler S, Wu L, Li R (2003) Spontaneous cell polarization through actomyosin-based delivery of the Cdc42 GTPase. *Science* 299(5610):1231–1235.
10. van der Gucht J, Sykes C (2009) Physical model of cellular symmetry breaking. *Cold Spring Harb Perspect Biol* 1(1):a001909.
11. Mullins RD (2010) Cytoskeletal mechanisms for breaking cellular symmetry. *Cold Spring Harb Perspect Biol* 2(1):a003392.
12. Howard J (2009) Mechanical signaling in networks of motor and cytoskeletal proteins. *Annu Rev Biophys* 38:217–234.
13. Cameron LA, Footer MJ, van Oudenaarden A, Theriot JA (1999) Motility of ActA protein-coated microspheres driven by actin polymerization. *Proc Natl Acad Sci USA* 96(9):4908–4913.
14. van Oudenaarden A, Theriot JA (1999) Cooperative symmetry-breaking by actin polymerization in a model for cell motility. *Nat Cell Biol* 1(8):493–499.
15. van der Gucht J, Paluch E, Plastino J, Sykes C (2005) Stress release drives symmetry breaking for actin-based movement. *Proc Natl Acad Sci USA* 102(22):7847–7852.
16. Munro E, Nance J, Priess JR (2004) Cortical flows powered by asymmetrical contraction transport PAR proteins to establish and maintain anterior-posterior polarity in the early *C. elegans* embryo. *Dev Cell* 7(3):413–424.
17. Grill SW, Kruse K, Jülicher F (2005) Theory of mitotic spindle oscillations. *Phys Rev Lett* 94(10):108104.
18. Chau AH, Walter JM, Gerardin J, Tang C, Lim WA (2012) Designing synthetic regulatory networks capable of self-organizing cell polarization. *Cell* 151(2):320–332.
19. Cramer LP (2010) Forming the cell rear first: Breaking cell symmetry to trigger directed cell migration. *Nat Cell Biol* 12(7):628–632.
20. Mseka T, Cramer LP (2011) Actin depolymerization-based force retracts the cell rear in polarizing and migrating cells. *Curr Biol* 21(24):2085–2091.
21. Gardel ML, Schneider IC, Aratyn-Schaus Y, Waterman CM (2010) Mechanical integration of actin and adhesion dynamics in cell migration. *Annu Rev Cell Dev Biol* 26:315–333.
22. Chan CE, Odde DJ (2008) Traction dynamics of filopodia on compliant substrates. *Science* 322(5908):1687–1691.
23. Barnhart EL, Lee K-C, Keren K, Mogilner A, Theriot JA (2011) An adhesion-dependent switch between mechanisms that determine motile cell shape. *PLoS Biol* 9(5): e1001059.
24. Gardel ML, et al. (2008) Traction stress in focal adhesions correlates biphasically with actin retrograde flow speed. *J Cell Biol* 183(6):999–1005.
25. Sabass B, Gardel ML, Waterman CM, Schwarz US (2008) High resolution traction force microscopy based on experimental and computational advances. *Biophys J* 94(1): 207–220.
26. Lee J, Leonard M, Oliver T, Ishihara A, Jacobson K (1994) Traction forces generated by locomoting keratocytes. *J Cell Biol* 127(6 Pt 2):1957–1964.
27. Fournier MF, Sauser R, Ambrosi D, Meister J-J, Verkhovsky AB (2010) Force transmission in migrating cells. *J Cell Biol* 188(2):287–297.
28. Wilson CA, et al. (2010) Myosin II contributes to cell-scale actin network treadmilling through network disassembly. *Nature* 465(7296):373–377.
29. Rubinstein B, Fournier MF, Jacobson K, Verkhovsky AB, Mogilner A (2009) Actin-myosin viscoelastic flow in the keratocyte lamellipod. *Biophys J* 97(7):1853–1863.
30. Ruoslahti E, Pierschbacher MD (1987) New perspectives in cell adhesion: RGD and integrins. *Science* 238(4826):491–497.
31. Straight AF, et al. (2003) Dissecting temporal and spatial control of cytokinesis with a myosin II Inhibitor. *Science* 299(5613):1743–1747.
32. Ishihara H, et al. (1989) Calcium-independent activation of contractile apparatus in smooth muscle by calyculin-A. *J Pharmacol Exp Ther* 2:388–396.
33. Guilluy C, Garcia-Mata R, Burridge K (2011) Rho protein crosstalk: Another social network? *Trends Cell Biol* 21(12):718–726.
34. Bell GI (1978) Models for the specific adhesion of cells to cells. *Science* 200(4342): 618–627.

Supporting Information

Barnhart et al. 10.1073/pnas.1417257112

SI Text

SI Computational Model of Adhesion Stick–Slip Mediated Symmetry Breaking of an Actomyosin Gel Myosin-Powered Retrograde Actin Network Flow

Experimental and theoretical studies have established that myosin contracts actin arrays and generates contractile stress and that this stress grows with increasing myosin concentration. We assume that the myosin stress is isotropic, consider it a scalar, and make the simplest assumption that the stress, kM, is linearly proportional to the myosin density. Here M is the myosin density and k is the proportionality coefficient (typical force per myosin unit). The contractile force applied to the actin network is the divergence of the stress, in this case, its gradient, $k\nabla M$. As in our previously published model (1), we assume that adhesion complexes generate viscous resistance to the flow of F-actin. The respective resistance force is given by $\zeta\vec{U}$, where ζ is the effective adhesion drag coefficient that we call adhesion strength and $\vec{U}$ is the velocity of F-actin flow in the laboratory coordinate system. The adhesion resistive force is balanced by the active contractile stress: $\zeta\vec{U} = k\nabla M$.

The simple equation $\zeta\vec{U} = k\nabla M$ does not take into account passive stresses in the F-actin network due to its deformation during the flow. To add these passive stresses, we follow ref. 1 and assume that these stresses have viscous character on the relevant time scale of tens of seconds. The small elastic component of the stress in the lamellipodium can be neglected (1), so we model a combination of the shear and deformation stresses in the F-actin with the formula $\left(\frac{1}{3}\mu + \mu_b\right)(\nabla \cdot \vec{U})I + \mu(\nabla\vec{U} + (\nabla\vec{U})^T)$, where μ and μ_b are the shear and bulk viscosities, respectively, and I is the identity tensor. Adding the divergence of these passive stresses to the myosin and adhesion forces results in the force balance equation determining the flow rate,

$$\left[\left(\frac{1}{3}\mu + \mu_b\right)\nabla\nabla \cdot \vec{U} + \mu\nabla^2\vec{U}\right] + k\nabla M = \zeta\vec{U}. \qquad \textbf{[S1]}$$

The boundary condition is the zero pressure at the free lamellipodial boundary,

$$\vec{n} \cdot \left[\left(\frac{1}{3}\mu + \mu_b\right)(\nabla \cdot \vec{U})I + \mu\left(\nabla\vec{U} + (\nabla\vec{U})^T\right) + kM\right] = 0, \qquad \textbf{[S2]}$$

where $\vec{n}$ is the local normal unit vector to the lamellipodial boundary. The model assumes that the F-actin viscosity is spatially constant, independent of the F-actin density, simplifying the analysis. A more detailed assumption of the viscosities being a function of the F-actin density does not change the qualitative pattern of the actin flow (1).

SI Adhesion Strength

Cell–substrate adhesion is mediated by the binding of adhesion molecules to both the actin network and the underlying substrate (2). Dynamic coupling of the actin network to the underlying substrate through populations of adhesion molecules generates a frictional slippage interface (3). Forces generated by myosin-driven actin network flow are transmitted to the substrate through this interface, resulting in traction force generation: $\vec{T} = \zeta\vec{U}$. The strength of cell–substrate adhesion in our model is characterized by the adhesion drag coefficient, ζ, which effectively describes the strength of the coupling between the actin network and the substrate. In principle, ζ is proportional to the density and the effective binding affinity of the bound adhesion molecules. Moreover, it has recently been shown that parameter ζ has a stick–slip-like behavior: Adhesion strength is strongest at low actin flow rates and weakens at high actin flow rates (4, 5). Our experimental measurements of actin network flow and traction forces are also consistent with stick–slip adhesion: Stationary keratocytes exert relatively large traction forces on the substrate despite low actin flow rates, whereas motile cells generate much smaller traction forces despite high actin flow rates. Thus, parameter ζ must decrease during symmetry breaking and motility initiation. We model the stick–slip behavior of adhesions, along with the dynamics of adhesion binding/unbinding, with the following equation:

$$\frac{\partial\zeta}{\partial t} = D_\zeta\nabla^2\zeta - \nabla \cdot \left(\left(\Theta\vec{U} - \nabla H(\vec{x} - \vec{x}_0) + \frac{\delta\vec{u}}{\sqrt{\zeta}}\right)\zeta\right) + f(\zeta) + s(u). \qquad \textbf{[S3]}$$

D_ζ is a diffusion constant describing the random unbinding/rebinding dynamics of the adhesion proteins about the steady-state density. Θ is a numerical parameter between 0 and 1 that describes the advection of the adhesion due to myosin-induced actin flow: It is 1 if the adhesion molecules flow with actin and 0 if the adhesion molecules are steadfast against the actin flow. This parameter plays a minor role in our model, so we will just set it to $\Theta = 0$. $H(\vec{x} - \vec{x}_0)$ is a position ($\vec{x}$) dependent function that expels the adhesion molecules from the center of the cell $\vec{x}_0$ where the nucleus is located. The precise form of the equation for expelling adhesion molecules is unimportant; we use the following function:

$$H(\vec{x} - \vec{x}_0) = \frac{h_0 \exp^{-|\vec{x} - \vec{x}_0|^2/r_0^2}}{1 + |\vec{x} - \vec{x}_0|^4/r_0^4}, \qquad \textbf{[S4]}$$

where r_0 represents the effective radius of the nucleus and h_0 is the effective repulsion strength. Presence of the nucleus in the simulations is not crucial for any qualitative model predictions. However, it makes resemblance between the simulated and real flow and myosin distributions much more striking. This is most apparent in the symmetric stationary cell (Fig. 1): The experiment shows that there is a "hole" in the myosin distribution at the center of the cell; without the nucleus in the simulations, myosin would accumulate exactly in the center of the cell.

We model the stick–slip behavior of adhesions phenomenologically using the functions $f(\zeta)$ and $s(u)$. Here $f(\zeta)$ is a function of adhesion strength ζ, and $s(u)$ is a function of the actin flow rate $u = |\vec{U}|$. We require that equation $f(\zeta) + s(u) = 0$ has one solution ζ_0 at low flow rate (small $u \gg u^*$) and a different solution ζ_1 at high flow (large $u \ll u^*$) for some critical flow rate u^*. For simplicity, we choose

$$f(\zeta) = -k_\zeta\left(\frac{1}{2}\tanh\left(\frac{\zeta - \zeta_0}{\Delta\zeta}\right) + \frac{1}{2}\tanh\left(\frac{\zeta - \zeta_1}{\Delta\zeta}\right)\right) \qquad \textbf{[S5]}$$

$$s(u) = -k_\zeta\left(\frac{(u/u^*)^2}{1 + (u/u^*)^2} - \frac{1}{2}\right) \qquad \textbf{[S6]}$$

where k_ζ corresponds to the switching rate and $\Delta\zeta$ adjusts the sensitivity of the dynamics to small perturbation about the stable values of ζ. Note that the stable values are ζ_0 when $u \ll u^*$ and ζ_1

when $u \gg u^*$, which is exactly what we need to model the stick–slip behavior. We have tested other sets of equations that satisfy the above conditions for equation $f(\zeta)+s(u)$, and the results are qualitatively the same. This model predicts the relation between the flow rate and traction stress, which is in semiquantitative agreement with the measurements (Fig. S5).

$\delta\vec{u}$ is a random driving term for studying the stability of the system in the presence of stochastic fluctuations; the $1/\sqrt{\zeta}$ factor is included in accordance with Eq. **S5**.

The boundary condition is

$$-\vec{n}\cdot\left(D_\zeta\nabla\zeta-\left(\Theta\vec{U}-\nabla H+\frac{\delta\vec{u}}{\sqrt{\zeta}}\right)\zeta\right)=\varepsilon^a_\pm V_\perp\zeta \qquad \textbf{[S7]}$$

where $\vec{n}$ is the outward normal at the cell boundary and $V_\perp$ is the velocity of the cell boundary. The left-hand side is the normal diffusion-advection flux. It is usually set to zero when the boundary is fixed ($V_\perp=0$). Because we are interested in watching how the shape evolves when $V_\perp\neq 0$, we need to add additional fluxes at the boundary due to the fact that the boundary is either retracting ($V_\perp<0$), causing the local adhesion density, and therefore ζ, to increase, or protruding ($V_\perp>0$), causing ζ to increase. $\varepsilon^a_\pm$ is a parameter for modulating the effect of this boundary–flux coupling, and it depends on the sign of $V_\perp$. For example, if we want the rear adhesion molecules to quickly disassemble when the rear boundary moves over them, then we can simply set $\varepsilon^a_-=0$ when $V_\perp<0$. In our model, we fix $\varepsilon^a_-=0$ when $V_\perp<0$ and $\varepsilon^a_+=1$ when $V_\perp>0$, which assumes that adhesions rapidly disassemble at the rear and that density of adhesions is locally conserved at the leading edge. Note that we used the dynamic equation for the adhesion strength to introduce the fluctuations of the adhesion strength through the fluctuations of the flow, and to "soften" the adhesion switch in time and space to avoid numerical instabilities. Otherwise, a simple algebraic relation like that shown in Fig. 2*A* is sufficient for the model.

SI Myosin Transport

Following ref. 1, we assume that myosin molecules bind and move with the F-actin network. Myosin molecules detach from the F-actin, diffuse in the cytoplasm, and reattach. Here, we assume that detachment and reattachment are rapid, in which case, the system of equations for the actin-associated and diffusing myosin molecules (1) reduces to just one equation for the actin-associated myosin. In this equation, the rapid cycles of the detachment, diffusion in the cytoplasm, and reattachment effectively result in slow diffusion of the actin-associated myosin added to the myosin movement due to coupling with the F-actin,

$$\frac{\partial M}{\partial t}=D_M\nabla^2 M-\nabla\cdot\left(\left(\vec{U}-\nabla H(\vec{x}-\vec{x}_0)+\frac{\delta\vec{u}_m}{\sqrt{M}}\right)M\right), \qquad \textbf{[S8]}$$

where D_M is the a diffusion coefficient for actin-bound myosin molecules, and $\delta\vec{u}_m$ is a random driving term similar to $\delta\vec{u}$ for adhesion.

The boundary condition for the myosin transport is similar to that for the adhesion strength ζ,

$$-\vec{n}\cdot\left[D_M\nabla M-M\left(\vec{U}-\nabla H(\vec{x}-\vec{x}_0)+\frac{\delta\vec{u}_m}{\sqrt{M}}\right)\right]=\varepsilon^m_\pm V_\perp M. \qquad \textbf{[S9]}$$

We choose $\varepsilon^m_-=0.5$ to account for the fact the F-actin cytoskeleton is partially disassembled once it reaches the rear, and we choose $\varepsilon^m_+=1$ to locally conserve the myosin number as the front moves forward. Because this choice of $\varepsilon^m_\pm$ does not conserve the myosin molecules and a small deviation (typically <0.001% of total number) is introduced at each time step, we devise an ad hoc procedure to renormalize the myosin density by uniformly putting back any excess or deficit every few time steps to ensure that the overall number is conserved. This step is not necessary in the case of ζ, since ζ is not conserved in our model.

SI Stochastic Fluctuations

The random fluctuation of adhesion is highly correlated in both time and space (6). The source of the fluctuation can be due to a myriad of factors including both thermal and driven sources. To broadly capture the overall behavior phenomenologically, we model the random forcing term $\delta\vec{u}$ using a Langevin-like equation,

$$\frac{\partial\delta\vec{u}}{\partial t}=-\gamma\delta\vec{u}+\vec{\eta}, \qquad \textbf{[S10]}$$

where $\vec{\eta}$ is a random vector satisfying the following statistics:

$$<\vec{\eta}(\vec{x},t)>\;=0 \qquad \textbf{[S11]}$$

$$<\vec{\eta}(\vec{x}_1,t_1)\cdot\vec{\eta}(\vec{x}_2,t_2)>\;=2\nu\delta(t_1-t_2), \qquad \textbf{[S12]}$$

and all of the higher moments vanish. Here ν gives the characteristic amplitude of the fluctuation, while γ is a decay constant that models the characteristic time duration of fluctuations. Since our system is not in equilibrium, we do not need to specify a fluctuation–dissipation relation between ν and γ. For spatially random fluctuation without any correlation, it is customary to choose $\nu(\vec{x}_1,\vec{x}_2)=\nu_0\delta(\vec{x}_1-\vec{x}_2)$. Specifically, we divide the space into little infinitesimal boxes and assign a random value to $\vec{\eta}(\vec{x})$ for each little box with variance ν_0. To build finite-size spatial correlations, all we have to do is to make the little boxes bigger, so that all $\eta(\vec{x})$ within each box share the same (albeit random) value. Mathematically, this transformation can be done smoothly (so that it can be easily handled numerically) by fast Fourier transform

$$\delta(\vec{x}_1-\vec{x}_2)=\frac{1}{4\pi^2}\int_{-\infty}^{\infty}\mathrm{d}k_x\int_{-\infty}^{\infty}\mathrm{d}k_y\exp^{i\vec{k}\cdot(\vec{x}_1-\vec{x}_2)} \qquad \textbf{[S13]}$$

and then restricting the integration to finite range so that k_x and k_y integrate over $[-2\pi/\Delta L, 2\pi/\Delta L]$, where ΔL is the desired box size or the correlation length. The final expression for the (two-point) correlation function is

$$<\vec{\eta}(\vec{x}_1,t_1)\cdot\vec{\eta}(\vec{x}_2,t_2)>\;=\frac{\nu_0}{2\pi^2}\int_{-2\pi/\Delta L}^{2\pi/\Delta L}\mathrm{d}k_x\int_{-2\pi/\Delta L}^{2\pi/\Delta L}\mathrm{d}k_y\exp^{i\vec{k}\cdot(\vec{x}_1-\vec{x}_2)}\delta(t_1-t_2). \qquad \textbf{[S14]}$$

In essence, this expression tells us to assign a random value to each Fourier mode with variance ν_0 and sum over all modes up to the cutoff.

SI Cell Dynamics

The cell boundary evolves kinematically according to the balance of the local forces and the net actin polymerization and retraction rates. The rate of displacement $V_\perp$ is

$$V_\perp(s)=\vec{U}(s)\cdot\vec{n}(s)+V_p(s)-\frac{2\tau_0}{R(s)} \qquad \textbf{[S15]}$$

where s is the arc length parameter marking the position along the cell boundary, $\vec{n}(s)$ is the outward-pointing normal vector, and $\vec{U}(s)\cdot\vec{n}(s)$ is the projected actin retrograde flow rate from Eq. **S1**.

V_p is the displacement rate due to actin polymerization, which we assume is made up of two components. One component is self-adjusted to conserve the area of the cell (after each step without this component, it is chosen in such a way that the total area of the cell does not change after the step); this component is a constant independent of the arc length parameter (s). Effectively, this is equivalent to the assumption that if the area increases above the target determined by plasma membrane availability, the membrane tension rises and slows down the polymerization rate. The second component accounts for the possibility that actin polymerization is graded along the leading edge due to the following effect: Higher myosin concentration locally either bundles actin filaments or disassembles them, thereby slowing the actin network growth. We assume that the polymerization is effective if the local myosin density is below some critical value M_0 and decreases at higher myosin density. We can model this behavior using Eq. **S16**,

$$V_p(s) = \frac{v_p^0}{1 + (M(s)/M_0)^2}. \qquad \textbf{[S16]}$$

In most simulations, we use only the first component, and the polymerization rate is constant along the cell edge. We add the second component only to investigate the possible role of the myosin–actin polymerization negative feedback reported in Fig. S2.

The final term in Eq. **S15** is the displacement due to the Laplace pressure from the membrane tension, which scales as the local curvature $1/R(s) = -\vec{n}(s) \cdot \partial_s \vec{n}(s)$. $\tau_0 = \sigma_0 l_0^2/\eta_0$, where σ_0 is the membrane tension, l_0 is a length scale of molecular dimension, and η_0 is the drag coefficient for the membrane as the surface evolves. In essence, the Laplace pressure, $2\sigma_0/R$, multiplied by l_0^2 gives us the total force on a patch membrane of size l_0^2. If we divide the total force $2\sigma_0 l_0^2/R$ by the drag coefficient associated with the patch of membrane, then we get the velocity at which the patch of membrane is moving. Note that τ_0 has the same dimension as diffusion constant.

SI Model Parameters

The model variables and parameters are listed in Table S2. Many of the parameter values are taken directly from our previous publications (1, 7), with minor recalibration to account for the newly obtain traction force data. For all model parameters, we checked that twofold to threefold variation of each parameter does not change qualitatively the predicted behavior. In other words, the model is robust to small variation of the parameter values. Here we list and discuss the physically relevant parameters.

SI Viscous Actin–Myosin Network

We take the characteristic length to be the typical radius of a cell $L_0 = 10$ μm (1, 7) and the characteristic speed to be the speed of a cell, $V_0 = 0.2$ μm/s (1, 7), which is comparable to the retrograde flow rate of the actin network. We set the shear viscosity $\mu =$ 5 kPa·s (8). The bulk viscosity is normally higher than the shear viscosity, as actomyosin gels are more resistant to compression than shear (1, 7), so we use the value $\mu_b = 100$ kPa·s (2, 10).

In our calculations, we multiply the viscosities by the characteristic thickness of the lamellipodium to convert the 3D stress derivatives into the 2D surface force densities. In order for the myosin stress to generate the observed flow of the order of $V_0 = 0.2$ μm/s inside a lamellipodium with characteristic thickness of $h \approx 0.2$ μm (9), the typical force scale is $\mu h V_0 = f_0 = 200\,pN$: In our calculations, we multiply the viscosities by the characteristic thickness of the lamellipodium $h = 0.2$ μm to convert the 3D stress derivatives into the 2D surface force densities. To nondimensionalize Eq. **S1**, we choose $k = \mu V_0 L_0 = 10$ nN based on dimensional analysis. Using this value of k, 100 units of myosin in our scheme is expected to generate an average force density on the order of $100k/L_0^3$ and hence is capable of generating an average traction force on the order of $100kh/L_0^3 \approx 20$ Pa, in agreement with our observations. For our runs, we use total amount of myosin $M_{total} = 100$ nondimensional units, or another myosin amount of the same order of magnitude, to investigate dependence of the frequency of the symmetry break at varying values of parameters. Note that M_{total} is conserved in the model. We set the diffusion constant $D_M = 0.8$ μm^2/s, which is sufficiently small to keep the dimensionless Peclét number $Pe = \frac{kM}{\zeta_0 D_M} > 1$ such that the actin flow dominates over diffusion (10).

SI Stick–Slip Adhesion

For runs with spatially constant adhesion, we set the adhesion drag coefficient (adhesion strength) $\zeta = 1.0$ nN·s·μm^{-4} as in ref. 7. Otherwise, we impose the stick–slip adhesion using Eq. **S3**. At low flow rates, the effective adhesion strength is strong, and, at high flow rate, adhesion slips and weakens (4). We set the low flow adhesion strength equal to $\zeta_0 = 2$ nN·s·μm^{-4}, which is comparable to the medium adhesion used in ref. 7, and set the weaker strength value at higher flow equal to $\zeta_1 = 0.03$ nN·s·μm^{-4}, comparable to the low adhesion strength. Since the typical speed of a moving keratocyte is $V_0 \sim 0.2$ μm/s and the cell thickness is $h \approx 0.2$ μm, as noted above, we expect the maximum traction force in our model to be on the order of $\zeta_0 h V_0 \approx 80$ Pa, comparable to the experimentally measured traction force in this study and others (5).

As we expect the adhesions to stay highly localized, we choose the adhesion diffusion coefficient $D_\zeta = 0.6$ μm^2/s, which is smaller than D_{M}. A key parameter to model the stick–slip adhesion is the critical flow rate u^* that demarcates the transition between low adhesion and high adhesion strength. According to our observations, $u^* \approx$ 0.1–0.2 μm/s, so we set $u^* = 0.1$ μm/s. k_ζ has dimension of (adhesion strength)/(time); it is of the order of magnitude of characteristic low adhesion strength (between ζ_0 and ζ_1) divided by the characteristic time of the adhesion turnover. We choose this characteristic low adhesion strength to be 0.1 nN·s·μm^{-4}, and we choose the characteristic turnover rate of 1/s (11); hence $k_\zeta = 0.1$ nN·μm^{-4}. The parameter $\Delta\zeta$ is a measure of the response of the system to deviation from steady state ζ; it dictates how easy it is to perturb the system. We choose $\Delta\zeta = 0.1$ nN·s·μm^{-4}, 5% of ζ_0, which allows the system to deviate by a reasonable amount but not too much.

SI Nucleus

The diameter of the nucleus is $r_0 \approx 7.5$ μm (7). To effectively repel both myosin and adhesion from the region where the nucleus resides, we need to choose $h_0 \exp(1)/r_0 \approx |\nabla H|_{|\vec{x}-\vec{x}_0|=r_0} > V_0$ for the repulsion to be strong enough to counteract the actin flow; we therefore use $h_0 = 1$ μm^2/s, which yields $h_0 \exp(1)/r_0 \approx 0.35$ μm/s.

SI Dynamic Fluctuations

The precise temporal correlation in cellular systems is unknown, but since most cellular activities happen on the time scale of minutes, we choose the correlation time to be $\gamma^{-1} = 100$ s. As for the spatial correlation, based on the sizes of the traction force patches, we set $\Delta L = 5$ μm. Given the magnitude of the driving random force $\vec{\eta}$ is of the form $\nu = \nu_0 \delta(\Delta\vec{x}) \approx \nu_0/\Delta L^2$, we can expect $<\delta\vec{u} \cdot \delta\vec{u}> \approx 2\nu_0/\Delta L^2\gamma$ (12). ν_0 needs to be large enough to counteract the effect of diffusion in order for the fluctuation to persist. Since the diffusion flux is $|D_z \nabla z| \sim D_z <z>/L_0$ (where z denotes either ζ or M and angular backet, $<\cdot>$, denotes averages) and the flux due to random advection is $|\delta u|\sqrt{z} \approx \sqrt{2\nu_0 <z>/\Delta L^2\gamma}$, the constraint on ν_0 is

$$\nu_0 > \frac{\gamma \Delta L^2 D_z^2 <z>}{2L_0^2} = \beta <z>. \qquad \textbf{[S17]}$$

Note that because ν_0 depends on z, $\delta\vec{u}$ (Eq. **S3**) and $\delta\vec{u}_m$ (Eq. **S13**) will take on different dimensions. To clarify the notation, we shall reserve ν_0 to be the variance associated with adhesion strength and define ν_m to be the variance associated with myosin density. Now, the numerical prefactor is $\beta \approx 1 \times 10^{-3}\ \mu\text{m}^4/\text{s}^3$, since $D_z \approx 1\ \mu\text{m}^2/\text{s}$ regardless of what z is. For adhesion, we may choose $<z> = \zeta_0$, in which case, the estimate is $\nu_0 > 0.01\ \text{nN/s}^2$; our simulation uses $\nu_0 = 0.1\ \text{nN/s}^2$. For myosin, if we let $<z> = <M>$, then the constraint is $\nu_m > 10^{-4}\ \mu\text{m/s}^3$. We are using $\nu_m = 8 \times 10^{-5}\ \mu\text{m/s}^3$.

SI Cell Shape Dynamics

The dynamics of the cell boundary is dictated by the balance of net local protrusion/retraction rate and the effective Laplace pressure. The strength of the Laplace pressure term is governed by $\tau_0 = \sigma_0 l_0^2/\eta_0$. The typical value of membrane tension (σ_0) in keratocytes is ~0.1–0.5 nN/μm (13), and the drag coefficient for the membrane η_0 scales as $\sim 6\pi\mu_0 l_0$, using Stoke's Law, where $\mu_0 = 1$ centiPoise is the viscosity of water. As for l_0, it should be the size of lipid molecule, ~1 nm. Using these numbers, $\tau_0 \sim 0.5\ \mu\text{m}^2/\text{s}$, which we use in this work. The values of additional parameters $\varepsilon^a_\pm$ and $\varepsilon^m_\pm$ are explained above. The values of parameters v^0_p and M_0 that are unknown from the experiment are chosen to produce the observed cell speed and shape aspect ratio.

SI Results

Free-Boundary Simulations Indicate That Adhesion Stick–Slip Is Required for Realistic Symmetry Breaking and Motility Initiation. We performed free-boundary simulations to determine whether the model —which incorporates both positive feedback between myosin and actin flow and negative feedback between adhesion and actin flow—can switch a stationary cell to a persistently motile state after acute perturbation of either adhesion or myosin. In these simulations, we initialized the computation with a circular, stationary cell with fixed area ($A = 600\ \mu\text{m}^2$) and uniformly distributed adhesion ($\zeta = \zeta_0$) and myosin ($M = M_{total}/A$). We fixed the cell boundary for the first 2 min of the simulation to allow the myosin density and actin flow patterns to equilibrate according to Eqs. **S1**, **S2**, **S8**, and **S9**. Then, we either decreased the adhesion strength (by setting $\zeta = \zeta_1$) or increased the myosin density (by setting M 20-fold higher than the average density) on one side of the cell ($t = 0$, Fig. 2 *C* and *D*). We then allowed the myosin density, adhesion strength, and actin flow patterns to evolve according to Eqs. **S1–S9** for 60 s before releasing the cell boundary ($t = 60$ s, Fig. 2 *C* and *D*). The position of the cell boundary then moved according to Eq. **S15**. For these simulations, we assumed that the actin polymerization rate remains constant during symmetry breaking and set $V_p(s) = v^0_p$. Transient perturbation of either adhesion or myosin resulted in rapid movement of a fan-shaped cell ($t = 350$ s, Fig. 2 *C* and *D*). The simulated myosin, actin flow, and traction force patterns recapitulated the patterns observed experimentally (compare Fig. 1 with Fig. 2 and Fig. S4). Specifically, in stationary cells, myosin localized to a ring around the cell body, and radially symmetric, slow actin flow rates generated radially symmetric, high-traction forces. In motile cells, myosin localized to two discrete spots on either side of the cell body, and fast actin flow rates in the cell rear generated relatively small traction forces.

Next, to determine whether negative feedback between adhesion and actin flow is required for symmetry breaking in our model, we performed free-boundary simulations in which large, transient perturbations of adhesion strength or myosin density were amplified by positive feedback between myosin and actin flow alone. These simulations were carried out as described, except that adhesion strength was held constant ($\zeta = \zeta_0$) throughout the simulations, rather than evolving according to Eqs. **S3–S7**. In these simulations, transient perturbations of adhesion or myosin resulted in persistently polarized, motile cells (Fig. S1). However, these simulated motile cells were round and slow moving rather than fan-shaped and fast-moving like real cells. Moreover, the simulated myosin, actin flow, and traction force patterns were inconsistent with our experimental observations: Actin flow rates were just slightly increased in the cell rear relative to the cell front, and myosin densities and traction forces were enriched along the entire length of the trailing edge, rather than at two discrete spots as observed experimentally. These simulations suggest that positive feedback between myosin and actin flow is not sufficient for switching round, stationary cells to a fan-shaped, rapidly moving state.

To determine whether an alternative negative feedback loop, other than negative feedback between adhesion and actin flow, could be induce realistic symmetry breaking and motility initiation, we performed simulations with negative feedback between myosin density and actin polymerization rates. This negative feedback is based on two experimental observations: Actin polymerization rates are higher at the front of motile keratocytes where there is little myosin (14), and myosin contraction promotes actin depolymerization (14, 15). This negative feedback was modeled using Eq. **S16**. The addition of this negative feedback loop was sufficient for initiation of rapid cell motility after a transient increase in myosin density (Fig. S2), but the simulated traction force pattern in motile cells was qualitatively different from the pattern observed experimentally. Specifically, large traction forces were localized along the entire length of the trailing edge in the simulated cells, rather than at just two spots on either side of the cell body, as in real cells. Altogether, these simulations suggest that an actin flow-dependent, nonlinear switch in adhesion strength is required for realistic symmetry breaking and motility initiation in keratocytes. All of the free-boundary simulations will therefore incorporate negative feedback between adhesion and actin flow, as well as positive feedback between myosin and actin flow, and actin polymerization will be set to a constant rate ($V_p(s) = v^0_p$).

Stochastic Fluctuations in Adhesion- and Myosin-Dependent Actin Flow Drive Spontaneous Symmetry Breaking. In the simulations in the deterministic model, symmetry breaking is the result of relatively large and long-lasting asymmetries in either adhesion strength or myosin density, added as external triggers to the model. To determine whether stochastic fluctuations can trigger spontaneous symmetry breaking in our model, we added fluctuations to our simulations. As in the simulations in the deterministic model, we initialized the computation with a circular cell with fixed area and uniformly distributed myosin and adhesion. The cell boundary was fixed for the first 2 min of the simulation to allow the myosin, adhesion, and actin flow patterns to equilibrate according to Eqs. **S1–S9** (Fig. S3, "Stationary" column). Then, stochastic fluctuations were added according to Eqs. **S10–S14**, and the cell boundary was released and allowed to move according to Eq. **S15** (Fig. S3, "Transient" column). These simulations resulted in the initiation of rapid, persistent motility (Fig. S3, "Motile" column). Traction force, actin flow, and myosin distributions around the perimeter of these simulated cells were comparable to distributions measured for real cells (compare Fig. S4 *A–C* and Fig. 1 *F*, *G*, and *I*).

The fluctuations in our model are characterized by three parameters: amplitude ν (ν_0 for adhesion fluctuations and ν_m for myosin fluctuations), the decay constant γ that gives the characteristic time duration of the fluctuations, and the spatial correlation scale ΔL. To determine how these parameters contribute to symmetry breaking, we performed free boundary simulations in which we varied ν, γ, and ΔL independently. For a given parameter set, we ran simulations for 50 s after the cell boundary was released and determined the fraction of cells that remained stationary versus breaking symmetry and initiating motility. Cells that moved more than 10 microns with the 50-s window were determined to have initiated motility. For simulations run with the parameters listed in Table S2 ($\nu_0 = 0.1\ \text{nN/s}^2$, $\nu_m = 8 \times 10^{-5}\ \mu\text{m/s}^3$, $\gamma = 1/100$ s, and $\Delta L = 5\ \mu\text{m}$), ~85% of simulations resulted in motility initiation (40 out 47 simulations); simulated cells that initiated motility tended to have larger fluctuations in traction forces before initiation (Fig. S6*A*), consistent with our experimental observations (Fig. S6 *C* and *D*). Reducing the amplitude of the fluctuations (i.e., reducing both v_0 and v_m) to 20% of the values listed in Table S2 prevented motility initiation. Increasing the fluctuation decay rate from 1/100s to 1/25s also prevented motility initiation. To systematically explore how the spatial correlation scale affects symmetry breaking, we selected different harmonic modes by using a narrow band-pass filter to construct the fluctuation spectrum using Eqs. **S13** and **S14**. We normalized the energy spectral density of the fluctuations to keep the amplitude of the noise consistent for all spatial correlation scales. We found that reducing the correlation scale from 5 μm to 3 μm prevented motility initiation. Thus, fluctuations that persist for tens of seconds and span ~5 μm are required for symmetry breaking in our model.

The Balance Between Adhesion Strength and Myosin Contraction Controls Symmetry Breaking and Motility Initiation. To determine how the relative levels of adhesion strength and myosin density contribute to symmetry breaking and motility initiation, we systematically varied ζ_0 (adhesion strength when actin flow is low) and M_{total} and determined whether the system remained stable or broke symmetry. The phase diagram for the system is shown in Fig. 5*B*. As expected, stationary cells were stable in simulations run with low M_{total} or high ζ_0 values; simulations run with high M_{total} or low ζ_0 values resulted in motility initiation. The phase transition occurs on a line with slope ~3.0/60 = 0.05 $\text{nN}\cdot\text{s}\cdot\mu\text{m}^{-4}$.

The nonlinear switch in adhesion strength is triggered when actin flow is greater than a critical threshold: $u > u^*$. We used this inequality to estimate the slope of the transition line between the systems that remain stable and those that break symmetry. Balancing the myosin force with the adhesion traction force, we estimate that $u \approx k|\nabla M|/\zeta_0$. We estimate ∇M *as* M_{total}/L_0^3 (myosin density M_{total}/L_0^2 divided by the cell size). Combining these, we get the following condition for when the system should break symmetry:

$$\zeta_0 < \zeta^* M_{total} \qquad \textbf{[S18]}$$

where slope $\zeta^* = k/(L_0^3 u^*) \approx 0.01\ \text{nN}\cdot\text{s}\cdot\mu\text{m}^{-4}$, comparable to our simulation result.

SI Experimental Methods

Keratocyte Culture. Keratocytes were cultured from the scales of the Central American cichlid *Hypsophrys nicaraguensis* as described (16). Briefly, scales were sandwiched between two acid-washed coverslips and cultured in Leibovitz's Media (L-15) supplemented with 14.2 mM Hepes pH 7.4, 10% (vol/vol) FBS, and 1% antibiotic–antimycotic at room temperature for 12–24 h. For the temperature shift and actin fluorescent speckle microscopy experiments and the traction force experiments, keratocytes were trypsinized and replated onto RGD peptide-functionalized glass coverslips or PAA gels, respectively. Cells were washed briefly with PBS and then treated with 0.1% trypsin and 1 mM EDTA in PBS for 5 min. The trypsin was quenched with a 10-fold excess of culture media, and the cells were transferred directly to RGD-coated surfaces and allowed to recover for 1 h. For all other experiments, individual stationary and motile cells were obtained from sheets of keratocytes that crawled off the scale by treating the cultures with 2.5 mM EGTA in 85% (vol/vol) PBS for 5 min. The cells were allowed to recover in full media for at least 20 min before imaging.

AlexaFluor546 phalloidin (AF546-phalloidin; Invitrogen) was used to label F-actin for fluorescent speckle microscopy. Two nanomoles of AF546-phalloidin was mixed with 7 μM dATP, 7 mM GTP, and 5 mM CTP in ddH_2O for 15 min at room temperature to prevent phalloidin aggregation. The phalloidin mixture was electroporated in keratocytes using a small-volume perfusion chamber with field stimulation (Warner Instruments) with three pulses at 180 V. Electroporated cells were allowed to recover for ~20 min before replating onto RGD-coated glass coverslips.

Preparation of PAA Gels for Traction Force Measurements. RGD-functionalized PAA gels embedded with fluorescent beads were generated following a modified version of previously published protocols (17, 18). First, 18 mm round glass coverslips were chemically activated to promote covalent attachment of the PAA gel to the glass (17). The coverslips were washed briefly with 0.1 M NaOH, air-dried, and then washed with 3-aminopropyltriethoxysilane for 5 min. After washing twice for 5 min in ddH_2O, the coverslips were washed with 0.5% glutaraldehyde in PBS for 30 min. The coverslips were then washed extensively with ddH_2O and air dried.

Next, a thin PAA gel with fluorescent beads embedded near the surface was polymerized on the activated glass coverslips (18). Stock solutions of 30% (wt/vol) acrylamide and 1% bis-acrylamide were diluted in ddH_2O to generate a 7.5% acrylamide, 0.05% bis-acrylamide solution. Tetramethylethylenediamine (TEMED) and ammonium persulfate (APS) were added to induce polymerization. Then 7 μL of the PAA solution were immediately pipetted onto a silanized glass slide, and a functionalized 18-mm glass coverslip was inverted onto the solution. The PAA was allowed to solidify under nitrogen for ~45 min. The glass coverslip, with attached PAA gel, was removed from the slide, and an additional 8 μL of 7.5% acrylamide/0.05% bis-acrylamide, this time containing a 1:100 dilution of 100-nm red fluorescent beads (Invitrogen), was pipetted on top of the PAA gel. A silanized 25-mm glass coverslip was placed on top, and the second PAA layer was allowed to solidify under nitrogen for ~45 min. After the PAA gel solidified, the gel–coverslip sandwich was placed in a 35-mm Petri dish filled with PBS, and the 18-mm coverslip, with attached gel, was gently pried away from the 25-mm coverslip. The gel was then washed extensively with PBS. This procedure yielded PAA gels ~30 μm thick with beads embedded in a thin layer at the surface of the gel. Acrylamide and bis-acrylamide concentrations and the TEMED to APS ratio were kept consistent with previously published papers, and we used published measurements of the shear modulus (19) for 7.5% acrylamide/0.05% bis—~1.5 kPa—in our traction force measurements.

Finally, the heterobifunctional crosslinker sulfosuccinimidyl 6-(4′-azido-2′-nitrophenylamino)hexanoate (sulfo-SANPAH) (Thermo Scientific) was used to crosslink RGD peptides to the surface of the gels. The gels were coated with 1 mg/mL sulfo-SANPAH, exposed to UV light for 5 min, and washed extensively with PBS. The gels were then coated with 1 mg/mL RGD peptides (RGDSK; Peptides International) and incubated overnight at 4 °C. The gels were washed twice with PBS and incubated with full media for ~30 min before plating cells.

Preparation of RGD-Functionalized Glass Coverslips. Glass surfaces coated with a range of RGD peptide densities were prepared as previously described (7). Briefly, poly(L-lysine)-[g]-poly(ethylene glycol) (PLL-PEG) and PLL-PEG-RGD were dissolved in PBS and mixed at various ratios, with a final total concentration of 500 μg/mL. The concentration of PLL-PEG-RGD was 1 μg/mL, 10 μg/mL, or 500 μg/mL for low, intermediate, and high adhesion strength surfaces, respectively. Glass coverslips were washed with acetone and isopropanol, coated with PLL-PEG/PLL-PEG-RGD for 20 min at room temperature with slow rocking, and thoroughly rinsed with ddH_2O. The surfaces were used immediately or stored for up to 24 h at 4 °C.

Pharmacological Treatments. Keratocytes were treated with 10–25 μM blebbistatin or 10 nM calyculin for 10–30 min before imaging. Local application of soluble RGD peptides was performed using a glass microneedle controlled by a micromanipulator, as described previously (7). The concentration of RGD peptides in the microneedle was 500 μg/mL. The RGD gradient steepness was controlled by generating fluid flow in the live cell chamber with a peristaltic pump connected to two needles on either side of the live chamber, ~1 cm apart and ~1 mm above the coverslip. Fluorescent dextrans were added to the microneedle along with soluble RGD peptides to visualize flow from the microneedle.

Temperature Shift Experiments. Motility initiation was induced by shifting the temperature from 20 °C to 30 °C, as previously described (16). The frequency of motility initiation was measured by counting the number of stationary cells that initiated motility within one hour of the temperature shift.

Immunofluorescence. Indirect immunofluorescence was performed using monoclonal mouse anti-vinculin and polyclonal rabbit anti-myosin. For vinculin staining, cells were fixed at room temperature with 4% formaldehye in 0.32 M sucrose in PBS for 15 min, permeabilized with 0.5% Triton X-100 for 10 min, and blocked with PBS-BT (3% BSA, 0.1% Triton X-100, and 0.02% sodium azide in PBS) for 30 min before incubation with primary antibody diluted in PBS-BT. For myosin staining, cells were extracted with 4% PEG and 1% Triton X-100 in cytoskeleton stabilizing buffer (50 mM imidazole, 50 mM KCl, 0.5 mM MgCl2, 1 mM EDTA, 1 mM EGTA, and 0.5 μM tetramethylrhodamine-phalloidin) for 5 min, rinsed three times with PBS, blocked with PBS-BT for 5 min, and then incubated with primary antibody diluted in PBT-BT. Cells were then fixed with 4% formaldehyde in PBS for 10 min.

Microscopy. Live cells were imaged on inverted microscopes (Diaphot-300; Nikon) using a 10× air objective (Nikon) for the temperature shift experiments, or a 40× N.A. 1.3 oil plan-Apo objective (Nikon) for local application of RGD peptides. Images were collected with a cooled back-thinned CCD camera (MicroMax 512BFT; Princeton Instruments) with a 2× optovar attached using MetaMorph software (Molecular Devices). Fixed cells were imaged on an inverted microscope (AxioObserver; Carl Zeiss MicroImaging, Inc.) using a 100× NA 1.4 total internal reflection fluorescence (TIRF) objective (Carl Zeiss MicroImaging, Inc). TIRF images were acquired using a 488-nm laser line and a motorized TIRF slider (Zeiss) to control the angle of incidence of the laser light. Images were collected with an EM-CCD camera (Hamamatsu) using AxioVision software (Zeiss).

Image Analysis. Movement of the actin network relative to the underlying substrate in AF546-phalloidin-speckled cells was tracked using an adaptive multiframe correlation algorithm as previously described (14, 16). This method assumes steady-state movement of the actin network with the area of the correlation template over the duration of the temporal window; thus, actin flow in fast-moving motile cells was accomplished by converting images from the laboratory frame of reference to the cell frame of reference as previously described (20). Flow tracking was then carried out in the cell frame of reference using five-frame averaging (10 s) and a correlation template between 11 × 11 pixels and 21 × 21 pixels (~1 × 1 microns to 2 × 2 microns). The resulting flow maps were then converted back to the laboratory frame of reference. In stationary cells, flow tracking was carried out in the laboratory frame of reference using 10-frame averaging (20 s).

1. Rubinstein B, Fournier MF, Jacobson K, Verkhovsky AB, Mogilner A (2009) Actin-myosin viscoelastic flow in the keratocyte lamellipod. *Biophys J* 97(7):1853–1863.
2. Gardel ML, Schneider IC, Aratyn-Schaus Y, Waterman CM (2010) Mechanical integration of actin and adhesion dynamics in cell migration. *Annu Rev Cell Dev Biol* 26:315–333.
3. Chan C, Odde D (2008) Traction dynamics of filopodia on compliant substrates. *Science* 322(5908):1687–1691.
4. Gardel ML, et al. (2008) Traction stress in focal adhesions correlates biphasically with actin retrograde flow speed. *J Cell Biol* 183(6):999–1005.
5. Fournier MF, Sauser R, Ambrosi D, Meister J-J, Verkhovsky AB (2010) Force transmission in migrating cells. *J Cell Biol* 188(2):287–297.
6. Digman MA, Wiseman PW, Choi C, Horwitz AR, Gratton E (2009) Stoichiometry of molecular complexes at adhesions in living cells. *Proc Natl Acad Sci USA* 106(7):2170–2175.
7. Barnhart EL, Lee K-C, Keren K, Mogilner A, Theriot JA (2011) An adhesion-dependent switch between mechanisms that determine motile cell shape. *PLoS Biol* 9(5):e1001059.
8. Bausch AR, Ziemann F, Boulbitch AA, Jacobson K, Sackmann E (1998) Local measurements of viscoelastic parameters of adherent cell surfaces by magnetic bead microrheometry. *Biophys J* 75(4):2038–2049.
9. Abraham VC, Krishnamurthi V, Taylor DL, Lanni F (1999) The actin-based nanomachine at the leading edge of migrating cells. *Biophys J* 77(3):1721–1732.
10. Bois JS, Jülicher F, Grill SW (2011) Pattern formation in active fluids. *Phys Rev Lett* 106(2):028103.
11. Digman MA, Brown CM, Horwitz AR, Mantulin WW, Gratton E (2008) Paxillin dynamics measured during adhesion assembly and disassembly by correlation spectroscopy. *Biophys J* 94(7):2819–2831.
12. Toda M, Kubo R, Saito N, Hashitsume N (1992) *Statistical Physics: Nonequilibrium Statistical Mechanics* (Springer, New York), 2nd Ed.
13. Lieber AD, Yehudai-Resheff S, Barnhart EL, Theriot JA, Keren K (2013) Membrane tension in rapidly moving cells is determined by cytoskeletal forces. *Curr Biol* 23(15):1409–1417.
14. Wilson CA, et al. (2010) Myosin II contributes to cell-scale actin network treadmilling through network disassembly. *Nature* 465(7296):373–377.
15. Reymann A-C, et al. (2012) Actin network architecture can determine myosin motor activity. *Science* 336(6086):1310–1314.
16. Yam PT, et al. (2007) Actin-myosin network reorganization breaks symmetry at the cell rear to spontaneously initiate polarized cell motility. *J Cell Biol* 178(7):1207–1221.
17. Wang Y-L, Pelham RJ, Jr (1998) Preparation of a flexible, porous polyacrylamide substrate for mechanical studies of cultured cells. *Methods Enzymol* 298:489–496.
18. Bridgman PC, Dave S, Asnes CF, Tullio AN, Adelstein RS (2001) Myosin IIB is required for growth cone motility. *J Neurosci* 21(16):6159–6169.
19. Fischer RS, Myers KA, Gardel ML, Waterman CM (2012) Stiffness-controlled three-dimensional extracellular matrices for high-resolution imaging of cell behavior. *Nat Protoc* 7(11):2056–2066.
20. Wilson CA, Theriot JA (2006) A correlation-based approach to calculate rotation and translation of moving cells. *IEEE Trans Image Process* 15(7):1939–1951.

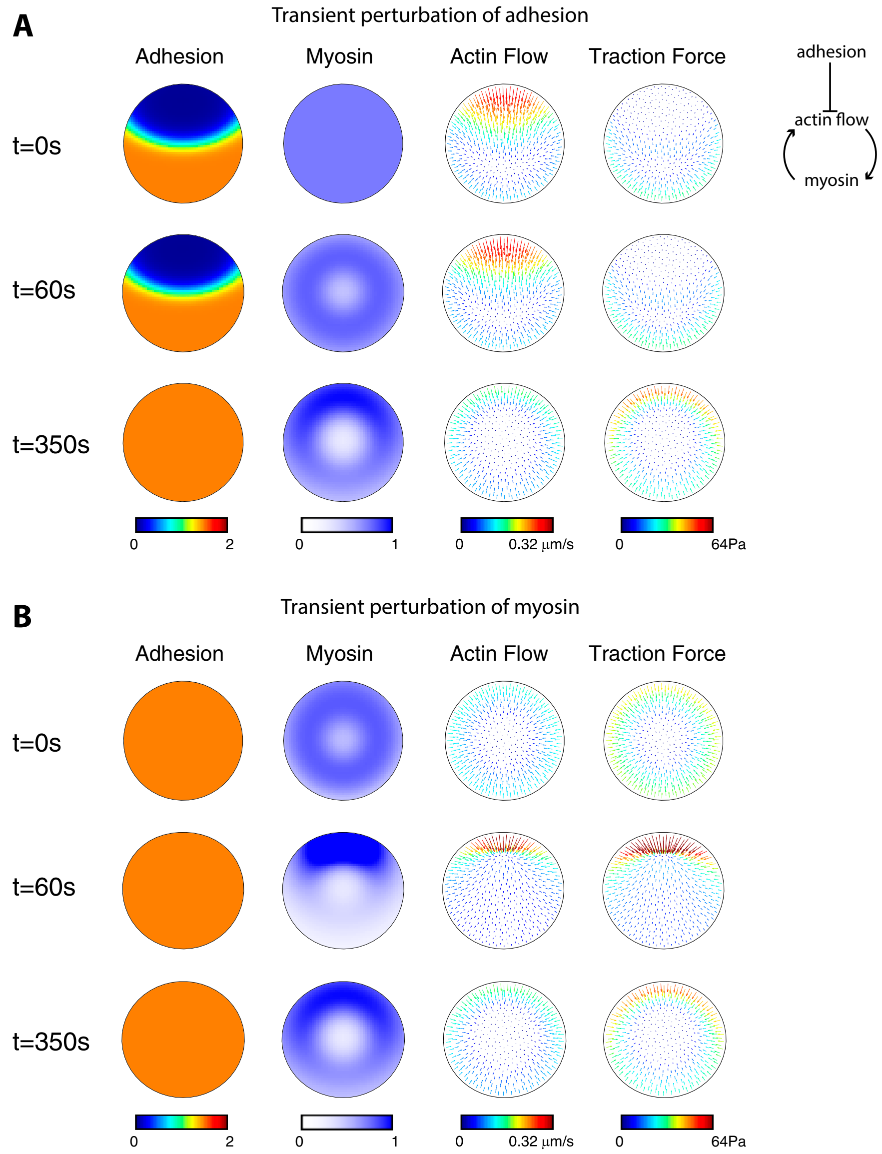

Fig. S1. Model simulations of transient perturbation of adhesion and myosin strength in the absence of negative feedback between adhesion and flow. Simulated adhesion, myosin, actin flow, and traction force distributions after transient perturbation of adhesion (*A*) or myosin (*B*). Simulations were carried out in the same manner as the simulations shown in Fig. 2, except that adhesion strength was held constant throughout the simulations ($\zeta = \zeta_0$). These simulations resulted in slow movement of circular cells, rather than rapid movement of fan-shaped cells, after the external asymmetries were removed.

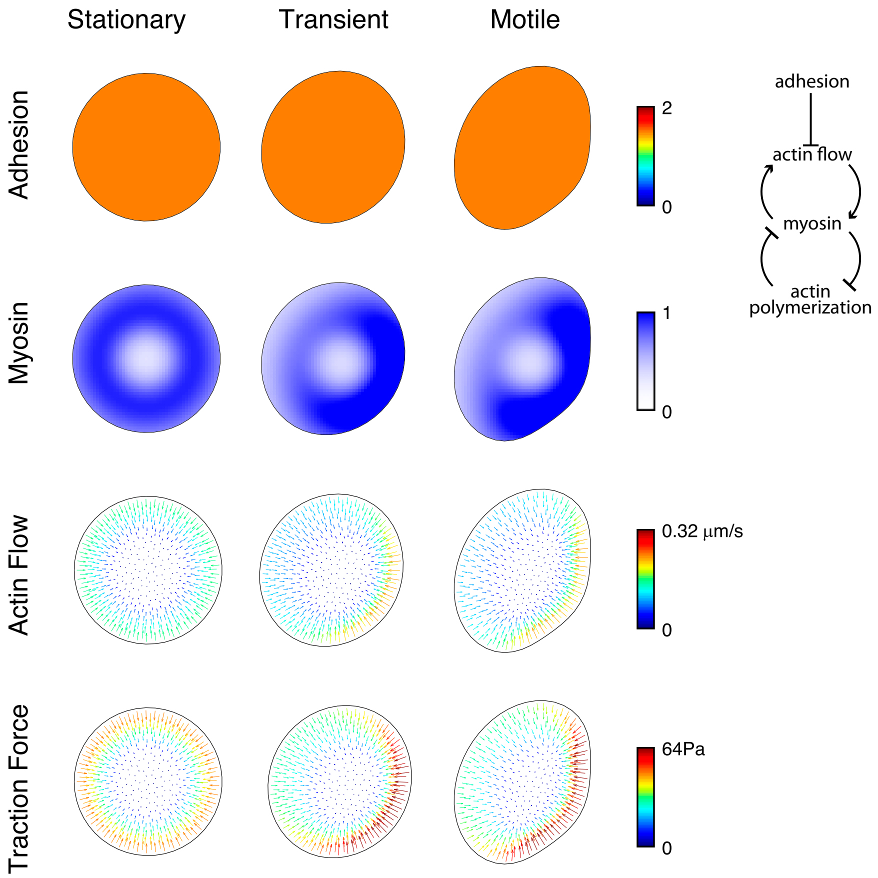

Fig. S2. Model simulations of transient up-regulation of myosin activity with negative feedback between myosin and actin polymerization. Simulated adhesion, myosin, actin flow, and traction force distributions after a transient increase in the myosin density on one side of the cell ("Transient" column). Simulations were carried out in the same manner as the simulations shown in Fig. 2, except that adhesion strength was held constant throughout the simulations ($\zeta = \zeta_0$) and negative feedback between actin polymerization and myosin localization was added (see *SI Text* for details). After the cell boundary was released, it was allowed to move according to the simulated actin polymerization pattern, as well as the simulation actin flow pattern. This simulation resulted in rapid movement of fan-shaped cells after the external myosin asymmetry was removed, but the traction force pattern in the motile cell was qualitatively different from the pattern observed experimentally (compare the traction force pattern in the "Motile" column to Fig. 1*A*).

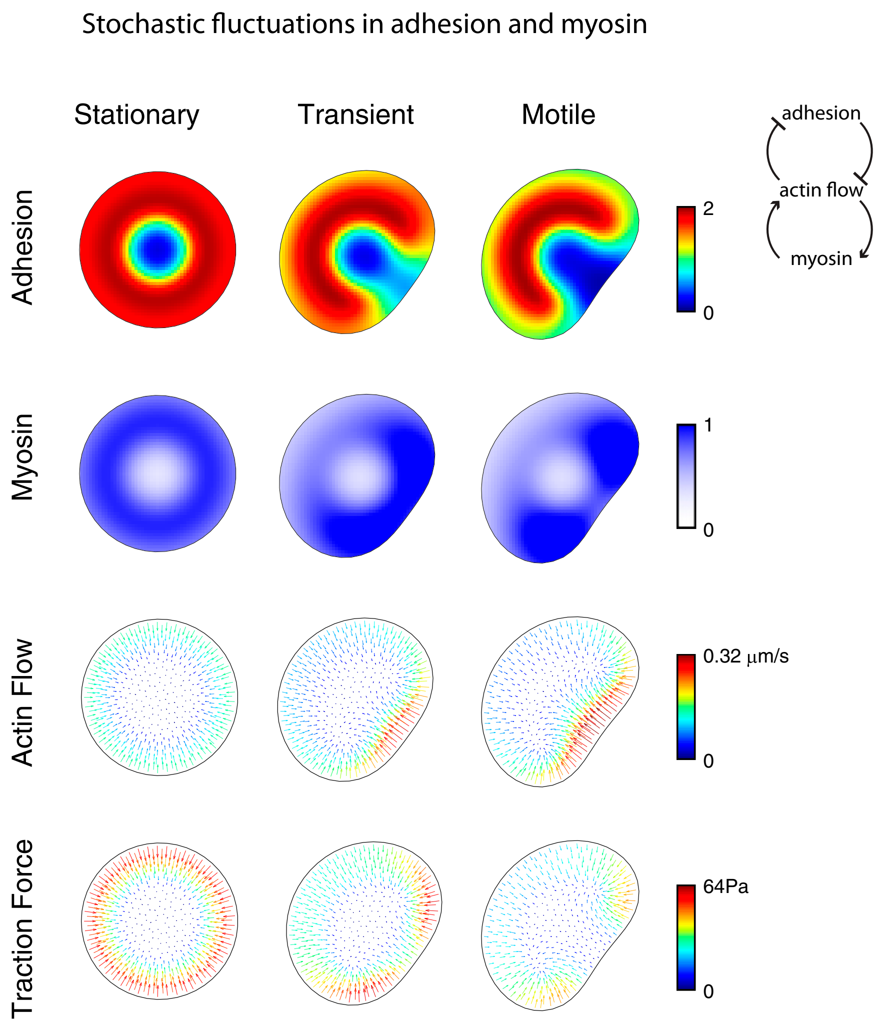

Fig. S3. Simulated stochastic fluctuations in adhesion- and myosin-dependent flow drive symmetry breaking and motility initiation. The simulation was initialized with a circular cell with fixed area and uniformly distributed myosin and adhesion. The cell boundary was fixed for the first 2 min of the simulation to allow the myosin, adhesion, and actin flow patterns to equilibrate ("Stationary" column). Stochastic fluctuations were added to the simulation (see *SI Text* for a detailed description), and the cell boundary was released and allowed to move according to the simulated actin flow pattern ("Transient" column). This simulation resulted in the initiation of rapid, persistent motility ("Motile" column).

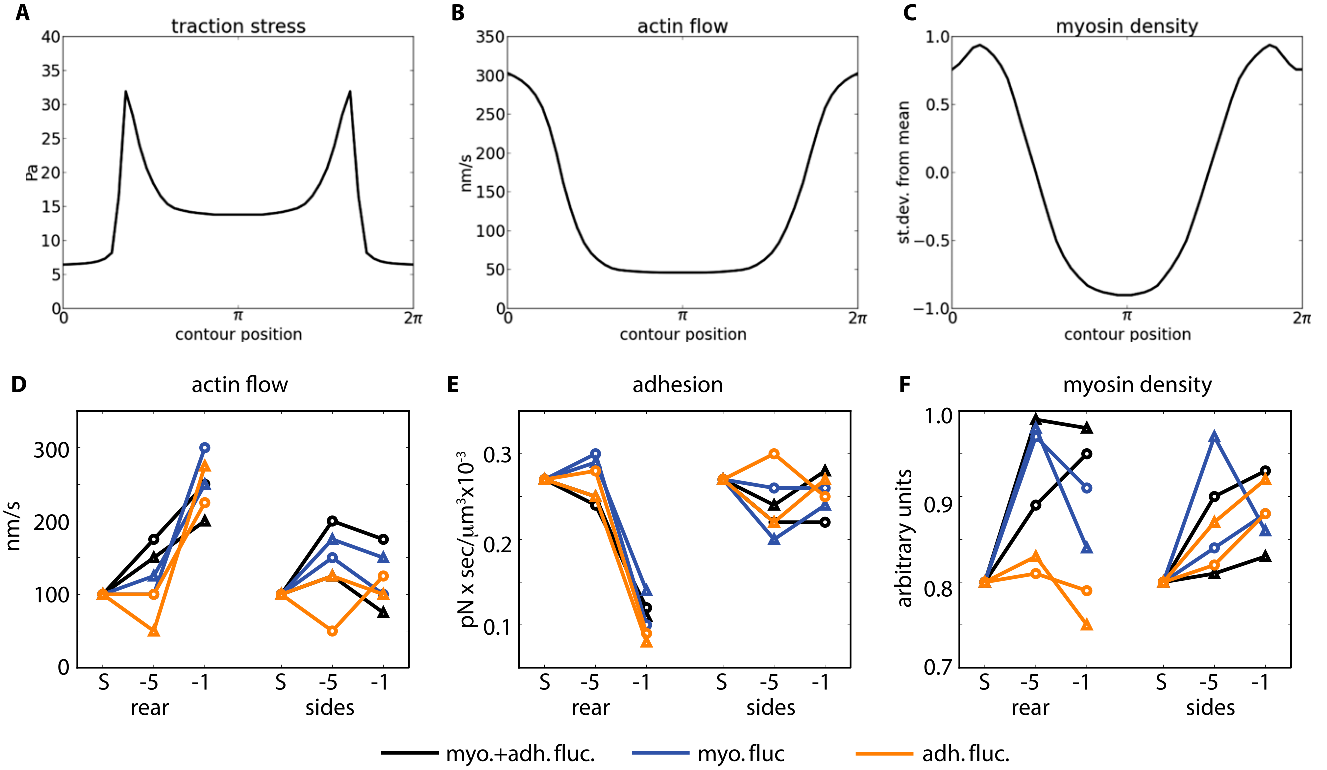

Fig. S4. Simulated traction stress, actin flow, and myosin distributions. (*A*–*C*) The traction stress (*A*), actin flow (*B*), and myosin density (*C*) in the simulated steadily moving cell (corresponding to 10 min of physical time after the simulations were started; after ~6–7 min, the cell shape and all distributions were not changing) are plotted as functions of the arc length around the cell boundary (π corresponds to the front; 0, 2π apply to the rear). The simulation corresponds to Fig. 2. The data from the simulation were taken from the grid points closest to the cell boundary. Myosin density was normalized in the same way as that in the experimental data reported in Fig. 1. (*D*–*F*) Actin flow (*D*), adhesion strength (*E*), and myosin density (*F*) measurements from six simulations. Stochastic fluctuations were added to actin flow in the dynamic equations for myosin localization (blue lines), adhesion strength (orange lines), or both (black lines). Measurements in the prospective cell rear and sides are plotted for the start of the simulation (S) and 5 min and 1 min before the onset of stable motility (–5 and –1, respectively). Myosin density was normalized in the same way as the experimental data reported in Fig. 1. The data were computed as local average in ~3 × 1 μm windows (longer side of the rectangle approximately parallel to the cell edge) in prospective rear and sides, respectively. Adhesion is reported in units of pN·s·μm^{-3} (units of pN·s·μm^{-4} multiplied by the lamellipodial thickness).

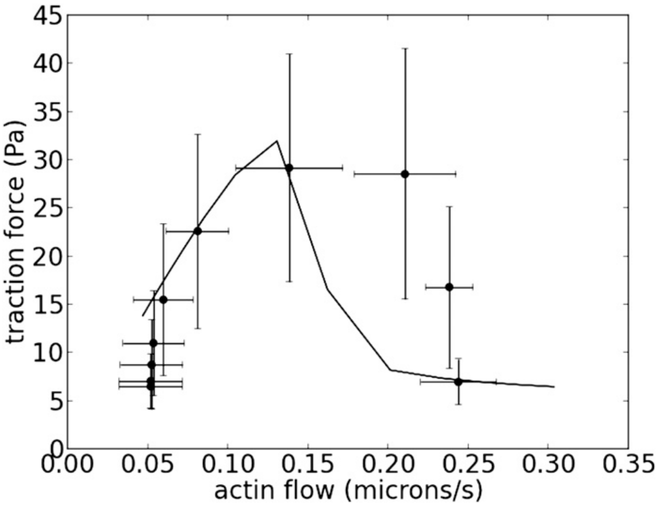

Fig. S5. Biphasic relationship between actin flow and traction force in motile keratocytes. Actin flow and traction forces were measured from model simulations (black line) and real cells (black circles) in motile cells at points around the cell perimeter. Traction forces increase with increasing actin flow from the center of the leading edge to the rear corners of the cells, but then decrease as actin flow increases farther from the rear corners to the center of the trailing edge. Error bars are SE.

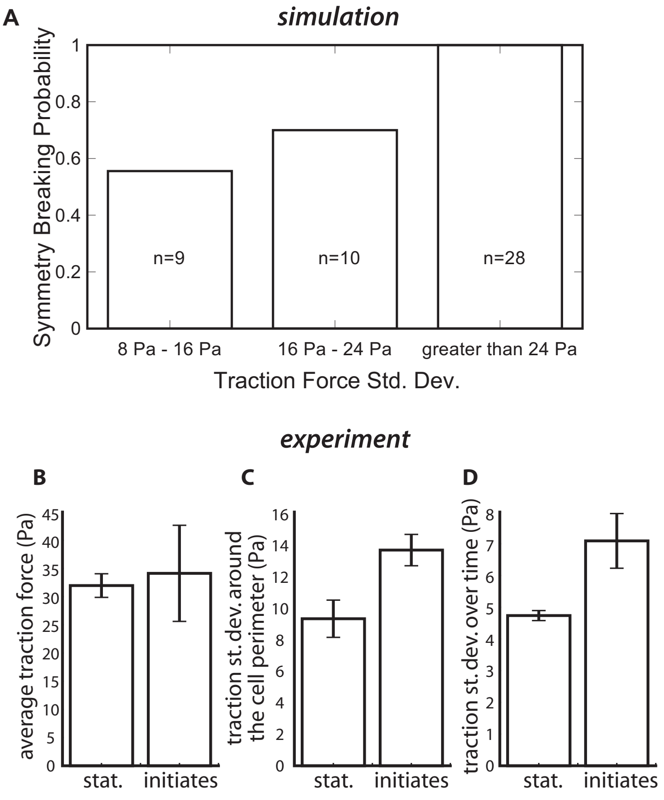

Fig. S6. Large traction force fluctuations are associated with an increased probability of symmetry breaking. (*A*) Model simulations; 47 simulations were carried out with stochastic fluctuations in adhesion- and myosin-dependent actin network flow using the parameters listed in Table S2. For each simulation, the SD of the traction force within 2.5 microns of the cell boundary over 100 s was computed while the cell was stationary, and the cells were binned according to the magnitude of the SD. We calculated the probability of symmetry breaking within each bin by dividing the number of motile cells within the group, at the end of the simulation, by the total number of cells in the group; these symmetry breaking probabilities are plotted for each bin. (*B*–*D*) Experimental measurements of average traction forces (*B*) and SD in traction forces around the cell perimeter in the first imaging frame (*C*) or at a single point on the cell perimeter over time (*D*) for cells that either remained stationary ("stat," *n* = 2) or initiated motility ("initiated," *n* = 4). Error bars are SEM.

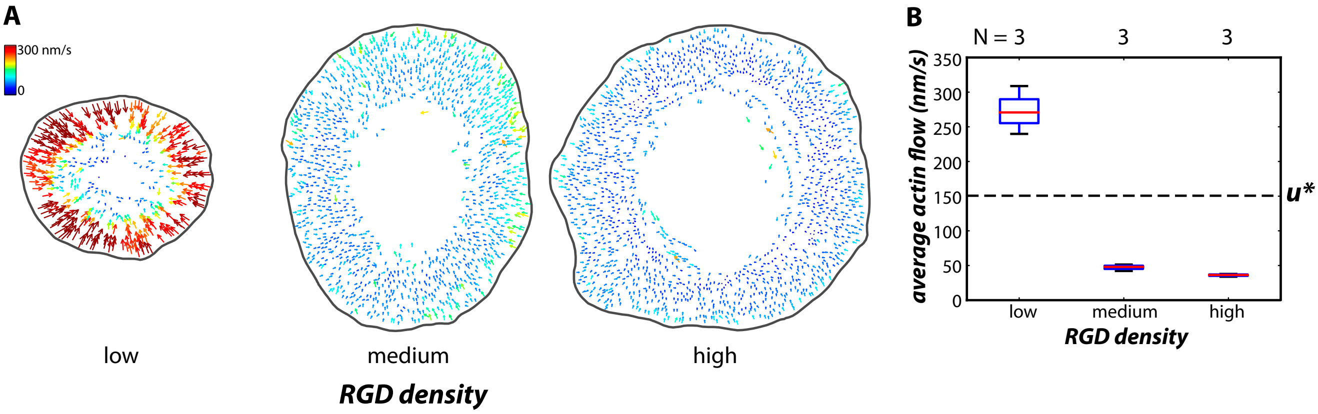

Fig. S7. Average actin flow rates in stationary cells increase with decreasing adhesion strength. (*A*) Representative actin network flow maps for stationary cells plated on surfaces coated with low, intermediate, and high densities of RGD peptides. The arrows indicate the direction and magnitude of flow. (*B*) Box plot showing average actin flow rates for populations of stationary cells. The plot shows the median value (red line), the 25th and 75th percentiles (lower and upper bounds), and measurements within 1.5 times the interquartile range (whiskers); $n = 3$ cells for each condition. The critical actin flow rate at which adhesions switch from sticking to slipping ($u^* = 150$ nm/s) in our model simulations is indicated by the dashed line.

Table S1. Model variables

Variable	Meaning	Dimension
t	time	s
$\vec{x}$	2D coordinate	μm
$M(\vec{x},t)$	myosin concentration	units/μm^2
$\vec{U}(\vec{x})$	local F-actin flow velocity	μm/s
$\vec{n}(\vec{x})$	local normal unit vector to the lamellipodial edge	nondimensional
$\zeta(\vec{x},t)$	adhesion strength/drag coefficient	nondimensional
$\delta\vec{u}(\vec{x},t)$	adhesion random advection	(nN·μm^{-2}·s)$^{1/2}$
$\delta\vec{u}_m(\vec{x},t)$	myosin random advection	μm$^{5/2}$/s
$V_\perp(s)$	net local protrusion/retraction rate	μm/s
$V_p(s)$	local polymerization rate	μm/s
$R(s)$	local radius of curvature	μm

Table S2. Constant model parameters

Parameter	Meaning	Value	Reference
V_0	characteristic cell speed	0.2 μm/s	(1, 7)
L_0	characteristic radius	10 μm	(1, 7)
h	cell thickness	0.2 μm	(9)
A	cell area	600 μm^2	(1, 7)
M_{total}	total myosin	~100 units	(7)
D_M	effective myosin diffusion coefficient	0.8 $\mu m^2/s$	(7)
D_ζ	adhesion strength diffusion coefficient	0.6 $\mu m^2/s$	assumed in this work
μ	shear F-actin viscosity	5 kPa·s	(8)
μ_b	bulk F-actin viscosity	100 kPa·s	(1, 7)
k	myosin force parameter	1 nN	dimensional analysis
h_0	nucleus repulsion strength	1 $\mu m^2/s$	this work
ε_+^a	adhesion boundary flux parameter for $V_\perp > 0$	1	this work
ε_-^a	adhesion boundary flux parameter for $V_\perp < 0$	0	this work
ε_+^m	myosin boundary flux parameter for $V_\perp > 0$	1	this work
ε_-^m	myosin boundary flux parameter for $V_\perp < 0$	0.5	this work
$u*$	critical flow rate	0.15 μm/s	this work
v_p^0	actin polymerization protrusion rate	0.25 μm/s	(1, 7)
M_0	critical myosin density for actin polymerization protrusion	0.033/μm^2	this work
ζ_0	adhesion strength at low flow rate	2 nN·s·μm^{-4}	this work; based on ref. 7
ζ_1	adhesion strength at high flow rate	0.03 nN·s·μm^{-4}	this work; based on ref. 7
$\Delta\zeta$	adhesion strength tolerance	0.1 nN·s·μm^{-4}	this work
k_ζ	adhesion turnover parameter	0.1 nN/μm^{-4}	this work
r_0	nucleus diameter	7.5 μm	(7)
ν_0	magnitude of adhesion fluctuation	0.1 nN/s^2	this work
ν_m	magnitude of myosin fluctuation	8×10^{-5} $\mu m/s^3$	this work
ΔL	correlated fluctuating length scale	5 μm	this work
τ_0	Laplace membrane tension parameter	0.5 $\mu m^2/s$	this work
γ	decay constant for the random fluctuation	1/100 s^{-1}	this work